Finite-size effects in Cu-Mn spin glasses

G. G. Kenning,* Jack Bass, W. P. Pratt, Jr., D. Leslie-Pelecky, Lilian Hoines, W. Leach, M. L. Wilson, R. Stubi,† and J. A. Cowen

Department of Physics and Astronomy and Center for Fundamental Materials Research, Michigan State University, East Lansing, Michigan 48824

(Received 2 August 1989; revised manuscript received 5 February 1990)

Finite-size effects in the spin glass (SG) Cu-Mn have been studied using magnetron-sputtered multilayer systems (MS's) of the form $Cu_{1-x}Mn_x$/Cu and $Cu_{1-x}Mn_x$/Si with $x=0.04$, 0.07, 0.14 (and some data for 0.21). The SG layers have widths $W_{Cu\text{-}Mn}$ ranging from 10 000 to 20 Å and are separated and magnetically decoupled from each other by interlayers of either 300 Å of Cu or 70 Å of Si. The MS's continue to show SG peaks in the zero-field-cooled (ZFC) "dc" magnetic susceptibility χ down to $W_{Cu\text{-}Mn}=20$ Å. The quasistatic freezing temperature T_f (defined as the location of the peak in χ) begins to decrease from its bulk value, T_f^b, at $W_{Cu\text{-}Mn}\approx 1000$ Å and approaches zero for SG thicknesses $0\leq W_{Cu\text{-}Mn}\leq 10$ Å with Cu interlayers or 30 Å $\leq W_{Cu\text{-}Mn}\leq 35$ Å with Si interlayers. A plot of the ratio T_f/T_f^b versus $W_{Cu\text{-}Mn}$ yields a separate "universal" curve for each of the two interlayer materials, independent of x. Structural analyses of the MS's using large- and small-angle x-ray diffraction, energy-dispersive x-ray spectroscopy, selected area diffraction, electron microscopic imaging, and parallel resistivity measurements, confirm that the samples are layered and indicate that interface intermixing is modest in the $Cu_{1-x}Mn_x$/Cu MS but more substantial in the $Cu_{1-x}Mn_x$/Si MS. This latter result suggests that the $Cu_{1-x}Mn_x$/Cu MS's are closer to isolated, uncontaminated layers of Cu-Mn, and further analysis thus focuses primarily upon these MS's. Various effects that might mimic size-dependent behavior are first considered, and then the "universal" variation of T_f/T_f^b with $W_{Cu\text{-}Mn}$ for the $Cu_{1-x}Mn_x$/Cu MS is analyzed in terms of (1) static finite-size scaling and (2) the activated dynamics of the Fisher and Huse cluster-excitation model. Appropriate parameters are derived for each model. This investigation is believed to be the first to examine how the properties of a long-range Ruderman-Kittel-Kasuya-Yosida SG such as Cu-Mn change as the lower critical dimension is crossed.

I. INTRODUCTION

There is great current theoretical interest in two phenomena: (1) finite-size scaling[1,2]—scaling behavior as a function of sample size in systems with one or more finite dimensions; and (2) the lower critical dimension d_l (Refs. 2 and 3)—the dimensional boundary across which a phase transition disappears. [For dimension $d>d_l$, the system of interest undergoes a thermodynamic phase transition at a critical temperature $T_c(d)>0$ K; by $d=d_l$, this temperature drops to $T_c=0$ K; for $d<d_l$, there is no transition.] While both phenomena have been investigated on a number of systems,[1,4–6] so far as we know, no investigations of either finite-size scaling or the crossover from three-dimensional (3D) to two-dimensional (2D) behavior in long-range, Ruderman-Kittel-Kasuya-Yosida (RKKY) spin glasses (SG's) had been published prior to the initial reports[7] of the current investigation. The interest in such measurements lies in the possibility of observing effects of dimensional crossover in a system involving long-range interactions between impurities that are inherently spatially disordered. Such systems are not yet well understood, so that experimental data are likely to simultaneously stimulate and focus new theoretical analysis.

In this paper we examine how the quasistatic spin-freezing temperature T_f of thin Cu-Mn SG layers decreases as the Cu-Mn layer thickness $W_{Cu\text{-}Mn}$ is reduced. In order to have enough SG material for accurate magnetic measurements, we fabricated sputtered multilayer samples (MS's) consisting of layers of Cu-Mn alternated with layers of a decoupling interlayer material thick enough to isolate the SG layers magnetically from each other. To check whether the behavior we observed was sensitive to the Mn concentration, we examined $Cu_{1-x}Mn_x$ samples with $x=0.04$, 0.07, 0.14, and, in a few cases, 0.21. To check whether different interlayers would yield similar results, we used both Cu and Si interlayers. The paper is organized as follows. In this Introduction we briefly review what SG's are and how current knowledge about them relates to this work. Section II describes sample preparation techniques and sample characterization. We shall see that adequate sample characterization is a difficult task, which we have approached from a variety of directions. Section III first reviews ways in which we could obtain spurious results, and then briefly describes three models to compare with our data. The first of these models, finite-size scaling, assumes a traditional phase transition. The second is a droplet excitation model stimulated in part by the report of our first results.[7] The third involves the possibility that Cu-Mn is not a traditional SG at all, but rather a short

coherence length spin-density-wave system. Section IV describes our magnetization studies on both $Cu_{1-x}Mn_x$/Si and $Cu_{1-x}Mn_x$/Cu samples. We find qualitatively similar data for the two different interlayers, but quantitative differences which we attribute to a combination of differences in the widths of the boundary layers in the two different MS's and penetration of the Si into the Cu-Mn along grain boundaries. From comparison of the structural characteristics of the two sets of samples, we conclude that the $Cu_{1-x}Mn_x$/Cu MS's more closely represent ideal thin SG layers. We compare the data for these MS's with the theoretical predictions, and then briefly mention recent dynamical studies of these same Cu-Mn MS's that support our interpretation of the data. Section V contains a summary and conclusions.

A. Spin glasses

SG's are magnetic systems with intrinsic spatial disorder (e.g., a random distribution of magnetic ions on the crystal lattice of a nonmagnetic host), which undergo a "spin-freezing" transition at a spin-freezing temperature T_f, but do not manifest long-range magnetic order.[3,8] The traditional experimental signature of a SG is a discontinuity in the slope (commonly called a cusp or a peak) of the "dc" magnetic susceptibility χ, coupled with an absence of any discontinuities at T_f in properties such as the heat capacity and the electrical resistivity. The location of the peak defines T_f. The SG state is not yet understood at a fundamental level, with much debate centering upon whether the spin-freezing transition is a true thermodynamic phase transition.[3] Recent measurements[9] showing divergences in nonlinear susceptibilities of the long-range SG Ag-Mn provide rather convincing evidence of a thermodynamic phase transition in 3D. On the other hand, T_f measured from the linear susceptibility χ is weakly dependent on the time t_m during which the measurement is made, so that only in the limit $t_m \to \infty$ is χ expected to behave as for a true phase transition. The measurements of χ described in this paper were made at a single measuring time, $t_m \sim 100$ sec, and we shall call the temperature T_f of the resulting peak the quasistatic freezing temperature. The primary issue we address is how T_f varies with the thickness $W_{\text{Cu-Mn}}$ films of the long-range SG Cu-Mn.

For theoretical analysis, SG's are usually divided into two classes, Ising-like (ISG), with an interaction Hamiltonian of the form $JS_{1z}S_{2z}$, and Heisenberg like (HSG), described by the Hamiltonian $J\mathbf{S}_1\cdot\mathbf{S}_2$.[3] It is useful to distinguish between systems in which J involves only short-range (e.g., nearest- and next-nearest-neighbor) or long-range [e.g., oscillatory RKKY (Ref. 3)] interactions. In metallic SG's, spin-orbit scattering of conduction electrons by impurities gives rise to an anisotropic (Dyazhosinki-Moriya) interaction between the SG impurities; in Cu-Mn, this anisotropy is small compared to the dominant RKKY interaction.[10,11]

Theoretical analyses[3] of ISG's predict that T_f will be finite for 3D and zero for 2D. The d_l for ISG's is thus predicted to lie between 3 and 2. In agreement with this prediction, recent data[12] on a 2D system believed to be an ISG indicate no SG phase transition at finite T_f.

In contrast, theoretical analyses[3] of 3D isotropic HSG's with only random nearest-neighbor interactions suggest that $T_f=0$ in 3D, which implies that the d_l lies above 3. Addition of anisotropy seems[3] to lead to a d_l below 3. A recent study of $Cd_{1-x}Mn_xTe$ (a HSG with short-range interactions) in the form of a superlattice with multilayers of $Cd_{1-x}Mn_xTe$/CdTe showed a broadening and disappearance of the susceptibility peak with decreasing $Cd_{1-x}Mn_xTe$ layer thickness.[13] Although these results are quite different from both simple theory[3] and the results for a long-range HSG that we present in this paper, they were interpreted as evidence for crossover from 3D to 2D behavior.

For an isotropic HSG with random long-range RKKY interactions, a recent calculation[14] suggests that $d_l \approx 3$. Experimental data have been used to argue that $d_l < 3$.[15]

In this paper we report measurements on Cu-Mn intended to study the behavior of χ across this presumed d_l boundary in a long-range RKKY SG in which anisotropic interactions are weak[10,11] compared to the RKKY interaction. We chose Cu-Mn for the following reasons. (i) Cu-Mn displays SG properties for Mn concentrations ranging from 4×10^{-3}% to 30%, with values of T_f from 10^{-4} K to 120 K; thus we have a wide temperature window in which to study the effects of crossover behavior. (ii) The metallic nature of Cu-Mn allows for convenient dc sputtering. (iii) Cu-Mn has been widely studied and is generally viewed as the prototypical RKKY SG with weak spatial anisotropy.[3] In addition to the work on the RKKY SG Cu-Mn described in this paper and its predecessors,[7] a study of finite-size effects of Au-Fe has also recently appeared,[16] and we have submitted a paper on Ag-Mn for publication.[17]

II. SAMPLE PREPARATION AND STRUCTURAL CHARACTERIZATION

A. The ideal MS and significance of deviations from the ideal

The ideal MS for the measurements we describe in this paper would have single-crystal layers with fixed widths, perfectly planar interfaces, and no chemical mixing at the interfaces. The structural characterization experiments we describe in this section of the paper show that our samples are layered, but that (i) the Cu-Mn and Cu layers are polycrystalline with crystalline sizes $\approx$400 Å in the $Cu_{1-x}Mn_x$/Cu MS and 40 to 200 Å in the $Cu_{1-x}Mn_x$/Si MS; (ii) the Si layers are amorphous; (iii) the layer widths fluctuate by several percent; (iv) the interface boundaries are irregular; and (v) there is some chemical mixing at the interfaces. Fortunately, a structurally ideal sample is not essential for observing the phenomena of interest in this paper. The first two of the listed deviations from the ideal should have no significant experimental consequences, since SG behavior is not sensitive to whether a sample is single crystal or polycrystalline, and amorphous

Si should still be quite appropriate for decoupling the SG layers. Since the interlayer widths have been chosen large enough to decouple the SG layers, fluctuations of a few percent in these widths should be unimportant, and fluctuations of the SG layer width by a few percent about its average value should average out in the determination of T_f. Irregular interfaces should also not be of great importance, so long as local variations in layer width are small compared to the widths themselves. This condition might be violated in our narrowest SG layers (i.e., $W_{\text{Cu-Mn}} \approx 20$ Å), particularly in the $Cu_{1-x}Mn_x$/Si MS, where we will see that both x-ray and parallel resistivity measurements suggest penetration of Si into the Cu-Mn layers along grain boundaries. Silicide formation might also occur in the $Cu_{1-x}Mn_x$/Si MS. Especially for the $Cu_{1-x}Mn_x$/Cu MS, the primary issue complicating the interpretation of our data is the last one, intermixing at the spin-glass–interlayer boundary. Such intermixing can result from the sputtering process itself, or from interdiffusion both during and after the sputtering process, phenomena we will examine in detail in Sec. II C 2 b.

Investigators who have studied the structures of metallic MS's deposited by both sputtering and evaporation techniques have inferred boundary intermixing widths ranging from 1 to 3 atomic layers[18,19] (which would correspond to 2–6 Å in our samples) in samples with bilayer widths of several atomic layers to, in one case, as large as 7–10 atomic layers[19] (14–20 Å in our samples) in samples with bilayer widths of 50 atoms or more. We will see that boundary widths of at least 35 atomic layers (70 Å) would be needed to spuriously produce the changes in T_f that we observe. Because the boundary intermixing widths found by different investigators vary with the deposition technique, the deposition rate, the substrate temperature during deposition, etc., we cannot use these results to draw any simple conclusions concerning our data, but must characterize our own samples as well as possible. Since one study[19] reported an increase in boundary layer width with increasing bilayer width in evaporated MS's, we must also examine whether such a phenomenon might be occurring in our data.

The primary technique used to study boundary widths in MS's is x-ray diffraction (XD), which also provides information about the bilayer periodicity d and about the sizes of crystallites in the samples. The main difficulty with this technique results from the fact that x-ray information cannot normally be deconvoluted to obtain a unique boundary profile; rather, parameters must be derived for an assumed profile. Discriminating between alternative profiles is especially difficult when (a) both the lattice parameters and scattering factors of the alternating layers are nearly the same—as is the case of our $Cu_{1-x}Mn_x$/Cu MS, or (b) when one of the layers is amorphous—as is the case for our $Cu_{1-x}Mn_x$/Si MS.

To provide background for understanding what we have and have not been able to learn about our samples, we briefly review the salient features of the theory of both large-angle (LAXD) and small-angle (SAXD) x-ray diffraction in MS's and examine how these will apply to our specific samples. For further details about x-ray scattering, see Refs. 20 and 21.

B. X-ray diffraction background

1. General background

The primary x-ray diffraction technique used to study MS's is Bragg reflection. The Bragg equation for scattering of x-rays from a set of parallel crystalline planes separated by the lattice parameter a' is

$$\sin\theta = (l\lambda/2)(1/a') , \tag{1}$$

where λ is the x-ray wavelength, and $l = 0, 1, 2, \ldots$ is the order of reflection. A measurement of the angle θ at which the lth-order reflection occurs yields $(1/a')$.

We consider a MS consisting of crystalline constituents with particular lattice planes oriented normal to the MS layers. The individual lattice parameters of the two constituents, a'_1 and a'_2, are periodic only within their own layers, so that the only true periodicity of the entire sample is the bilayer thickness $d = n_1 a'_1 + n_2 a'_2$, where n_1 and n_2 are the number of atoms of metal 1 and metal 2 in a bilayer. Strictly speaking, it is only $(1/d)$ which appears in Eq. (1) and determines the location of the reflection peaks. Since $(1/d)$ is much smaller than $(1/a'_1)$ and $(1/a'_2)$, the Bragg reflection peaks for a MS begin at much smaller angles than those for a single crystal.

If the individual metallic layers of the MS are many atoms thick, then several Bragg reflection peaks for $(1/d)$ will occur near the angles where Bragg reflections would be expected for $l(1/a'_1)$ or $l(1/a'_2)$ alone. These peaks turn out to be enhanced in such a way as to give strong "main peaks" at the appropriate angles for (l/a'_1) and (l/a'_2) alone, surrounded by "satellite peaks" separated from the main peak and each other by the small changes in angle associated with successive values of $(1/d)$.[22]

If the individual layers are only a few atoms thick, the two main peaks associated with a given l coalesce into a single central peak at (l/a), where the "average lattice parameter" a is defined as

$$a = d/(n_1 + n_2) . \tag{2}$$

The simplest way to understand the x-ray pattern expected for a MS, and to illustrate both the capabilities and limitations of x-ray studies for our MS, is to consider a MS with equal layer widths of the two constituents in which both the scattering factor f and the lattice parameter a' vary sinusoidally within the MS. If these two quantities have extremal values $f = f_0(1 \pm \eta)$ and $a' = a(1 \pm \epsilon)$, respectively, then central x-ray peaks appear at the Bragg angles for (l/a), and each such peak has two satellites that are separated from it by (nearly equal) angles determined by $(1/d)$. If η and ϵ are small, the ratios of the intensities $I_\pm$ of the large-angle $(+)$ and small-angle $(-)$ satellites to the intensity I_l of the lth central peak are given by[20]

$$I_\pm / I_l = \tfrac{1}{4}\{[(d/a) \pm 1] l\epsilon \pm \eta\}^2 . \tag{3}$$

In Eq. (3), ϵ and η are both positive numbers in a MS where the maximum lattice parameter and the minimum scattering factor occur together.

We see from Eq. (3) that periodic variations in electron

density (measured in terms of η) give rise to satellites for all values of l, including $l=0$. Periodic variations in lattice parameter (measured by ϵ), in contrast, give rise to satellites only for $l>0$, with contributions that are enhanced relative to those for η by the ratio $(d/a)^2$ and also by l^2.

More complex a' and f profiles, such as square wave for f (e.g., atomically sharp interfaces) or trapezoidal waves (linearly varying interfaces of finite width) for either a' or f or both, give rise to more complex expressions for the satellite intensities and to additional (higher-order) satellites around each of the l central peaks.[19,23,24] Even so, Eq. (3) remains a good starting point for understanding the intensities of the first-order satellites whenever the Fourier expansion of a more complex profile is dominated by a single sinusoidal component (i.e., in MS's with nearly equal layer widths of the two constituents).

2. Background specific to our samples

a. $Cu_{1-x}Mn_x$/Si. In our $Cu_{1-x}Mn_x$/Si samples, we normally see several nice SAXD satellites, but no LAXD satellites.

The absence of LAXD satellites will be an important piece of evidence used to infer that the Si in our MS is amorphous, since random variations in d by only a few percent have been shown[25] to eliminate LAXD satellites in samples with alternating crystalline and amorphous layers.

The presence of multiple SAXD satellites clearly indicates chemical layering. We estimate the expected intensity of the first SAXD satellite in $Cu_{1-x}Mn_x$/Si using Eq. (3) and the atomic numbers Z of Cu ($Z_{Cu}=29$) and Si ($Z_{Si}=17$), since the Z of Mn ($Z_{Mn}=24$) is close to that of Cu. Neglecting corrections for the fact that we used Cu $K\alpha$ radiation[20], and for the different planer densities of the Cu and Si,[20] we find simply $2\eta\approx(29-17)/23\approx0.6$. The ratio of the intensity of the first SAXD satellite to the zero-order satellite is then $I_{\pm}/I_0\approx\frac{1}{4}(0.3)^2\approx0.02$. With such a ratio, one can generally observe several higher-order SAXD satellites. In principle, the relative intensities of these satellites can be used to characterize the chemical profile of the MS. Unfortunately, the combination of quite different Cu-Mn and Si layer widths in most of our $Cu_{1-x}Mn_x$/Si MS's, with the fact that the relative intensities of the higher-order SAXD satellites are very sensitive to minor irregularities in this layering,[26] precluded the derivation of reliable values of boundary widths for our $Cu_{1-x}Mn_x$/Si samples. In addition, in a three-component system such as $Cu_{1-x}Mn_x$/Si, the presence of layering between the dominant Cu and Si components does not prove that the Mn impurity is necessarily also layered. The SAXD measurements thus provide no direct measure of the Mn profile in the $Cu_{1-x}Mn_x$/Si. Because of these limitations on the information we could obtain from x-ray diffraction measurements, we have used alternative measurements to gather what additional information we can.

b. $Cu_{1-x}Mn_x$/Cu. In contrast to the $Cu_{1-x}Mn_x$/Si MS, no SAXD satellites are found in any of the $Cu_{1-x}Mn_x$/Cu MS's on which T_f measurements were made. LAXD satellites are seen in samples with Mn concentrations $\geq 7\%$, but these satellites are weak.

The SAXD satellites are absent for two reasons: (i) because η is small ($\eta\approx0.005$ for $Cu_{0.86}Mn_{0.14}$/Cu); and (ii) because $W_{Cu}=300$ Å means that $d\geq320$ Å, which is large. From Eq. (3) we see that $\eta=0.005$ leads to a first-order $l=0$ satellite intensity of only $I/I_0\approx\frac{1}{4}(0.005)^2\approx0.000\,006$, about $3\frac{1}{2}$ orders of magnitude smaller than for the $Cu_{1-x}Mn_x$/Si MS. Values of $d\geq320$ Å push this satellite to $2\theta\leq0.25°$, where it is lost in the direct x-ray beam. To overcome these two difficulties, we made some test $Cu_{1-x}Mn_x$/Cu MS's with smaller values of both $W_{Cu\text{-}Mn}$ and W_{Cu}, and we will show in Sec. II D that these samples did yield weak SAXD peaks.

LAXD satellites are present because ϵ is enhanced in Eq. (3) by the ratio (d/a), which is large in our samples. The satellites are weak because ϵ itself is small ($\epsilon\approx0.0075$ for $Cu_{0.86}Mn_{0.14}$/Cu).[27] As an example, for an equal layer thickness $Cu_{0.86}Mn_{0.14}$/Cu (40 Å/40 Å) MS, Eq. (3) predicts an intensity ratio of about $\frac{1}{4}(40)^2(0.0075)^2\approx0.02$ for $l=1$, and four times larger for $l=2$. Data for such an MS will be shown in Sec. II D. Note that when LAXD satellites are determined primarily by ϵ, derived boundary profiles are not necessarily chemical profiles, since two different lattice parameters will adjust to each other over several atomic planes, even across an atomically sharp chemical boundary.

C. Samples

1. Target production

The Cu-Mn sputtering targets were produced by alloying 99.9999% pure Cu and 99.99% pure Mn (obtained from Aesar, Inc.) in an induction furnace. The graphite crucible containing the Cu and Mn was coated with boron nitride to ensure that the carbon did not contaminate the sample. The entire assembly was pumped to 2×10^{-6} Torr in a quartz tube and backfilled with a mixture of 90% Ar and 10% H gas. We determined the Mn concentrations in the targets by comparing the spin-glass temperatures T_f for bulk shavings from the target with the known T_f-versus-concentration curve.[8] The Cu and Si targets were obtained commercially from Varian, Inc. The Si had a room-temperature resistivity greater than 10 Ω cm. The semiconducting properties of this target permitted dc sputtering at room temperature.

2. The sputtering system, sputtering control, and interdiffusion

a. The sputtering system. Sputtering was carried out in an ultra-high-vacuum (UHV) compatible, cylindrical stainless-steel chamber, which was initially pumped to $\leq2\times10^{-8}$ Torr. The pressure in the chamber was then raised to $\simeq2.5\times10^{-3}$ Torr by introducing ultrahigh-purity Ar into the system through Simard "Tri-Mag" sputtering sources. The atoms were sputtered onto substrates mounted on a substrate positioning and monitoring apparatus (SPAMA) located ≈10 cm above the

sputtering targets. The SPAMA held eight substrate holders containing two substrates each, allowing us to simultaneously prepare two samples of each MS, one for structural analysis and one for susceptibility measurements. To make the MS, a stepping motor controlled by an IBM AT positioned the SPAMA alternately over two sputtering sources for chosen periods of time. The substrate surface was normally the [100] face of Si, but generally similar results were also obtained with [111] Si, single-crystal sapphire, and cleaved NaCl.

Typical sputtering rates were 1–3 Å/sec for the Si targets and 5–16 Å/sec for the Cu-Mn and Cu targets, and were controlled to a few percent. For a sputtering rate of 10 Å/sec an upper bound on the gaseous impurity content per monolayer deposited by this system has been estimated to be 1.7%.[26] No evidence of Ar was found when the samples were examined in an analytical electron microscope. A complete description of the sputtering chamber, SPAMA, flow controllers, and source assembly is given elsewhere.[28]

Preferential sputtering of one type of target atom over another can occur in alloy targets.[29,30] We infer from the agreement between the SG transition temperatures of target shavings and those for "bulk" (5000–10 000 Å) sputtered films that there was little or no preferential sputtering in our Cu-Mn samples.

b. Sputtering control and layer interdiffusion. We indicated in Sec. II B that the size of the interfacial mixing zone in our samples is an important issue in the analysis of our data. We briefly describe here what we can say about such intermixing in the sputtering process itself and due to layer interdiffusion during and after sputtering.

Boundary mixing in the sputtering process: Boundary mixing in the sputtering process can be tested using two nearly immiscible metals, such as Cu and Ag,[31] since MS's formed by sputtering two such metals at room temperature or below should have negligible bulk metallic interdiffusion. As part of another experiment, we have recently been studying $Cu_{0.86}Mn_{0.14}$/Ag MS's, which should serve well for sputtering control tests with the Cu and Ag.

Figures 1 and 2 show LAXD scans (solid curves), taken with a Rigaku D/MAX-RBX diffractometer with a 12 kW Cu rotating anode, of 4000 Å thick $Cu_{0.86}Mn_{0.14}$/Ag (15 Å/15 Å) and $Cu_{0.86}Mn_{0.14}$/Ag (8 Å/8 Å) MS, respectively, grown on top of a 1000 Å buffer layer of Ag. The dashed curve in Fig. 1 is a computer calculation assuming a square-wave chemical profile containing seven atoms each of Ag and $Cu_{0.88}Mn_{0.14}$, a coherence length ≈ 150 Å, and choosing as fitting parameters only the height and location of the main peak. The Ag and Cu-Mn lattice parameters were taken from measurements on sputtered Ag and $Cu_{0.86}Mn_{0.14}$ films; the scattering factors for the Ag and Cu-Mn were corrected[21] for angular dependence, use of Cu $K\alpha$ x rays, Debye-Waller factors, and the different area densities of $Cu_{0.86}Mn_{0.14}$ and Ag. This model predicts satellites larger than those observed. There are two obvious explanations for this discrepancy, both based upon the fact that the prediction is dominated by the assumed changes in lattice parameter rather than changes in atomic scattering factors. If, in these narrow layers, the two metals adjust to each other so that the maximum change in lattice parameter is smaller than assumed, the satellite intensities will be reduced. Alternatively, they will also be reduced if substantial intermixing of the metals occurs. Equation (3) can be used to check this latter alternative. With the same lattice and scattering parameters used in the computer program, the sine-wave model of Eq. (3) predicts percentage intensities of the lower and

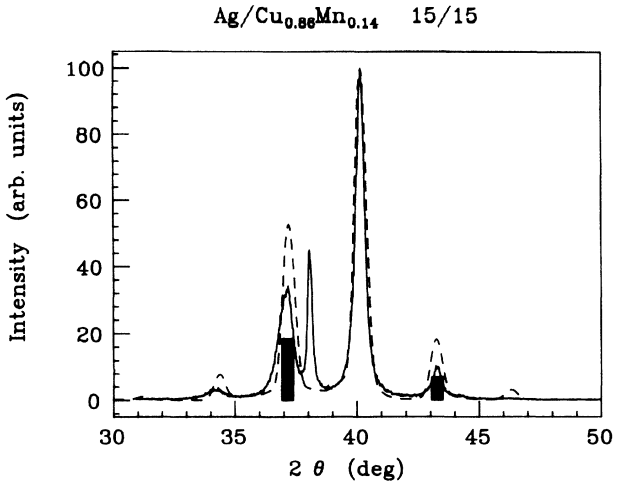

FIG. 1. LAXD scan for a $Cu_{0.86}Mn_{0.14}$/Ag (15 Å/15 Å) MS on a 1000 Å Ag buffer layer. The sharp peak at 38° and the small peak at 44.2° are Ag (111) and (200) peaks from the buffer layer. The dashed curve represents a computer-generated prediction for a square-wave chemical profile and coherence length ≈ 150 Å as described in the text. The filled bars indicate the relative satellite intensities predicted by the sine-wave model of Eq. (3).

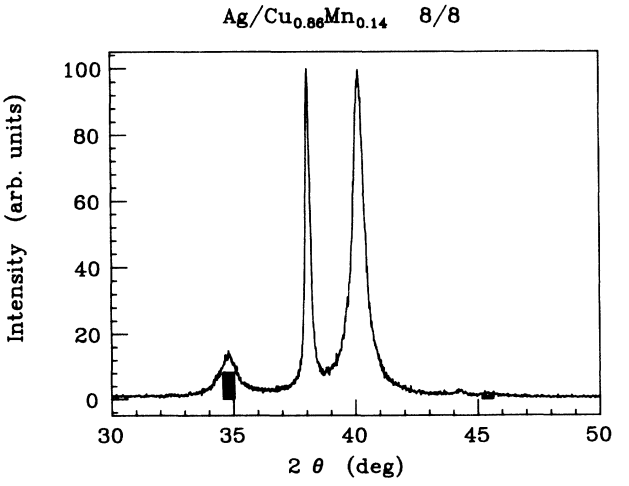

FIG. 2. LAXD scan for a $Cu_{0.86}Mn_{0.14}$/Ag (8 Å/8 Å) MS on a 1000 Å Ag buffer layer. The peaks at 38° and 44.2° are from the Ag buffer layer. The filled bars represent the relative satellite intensities predicted by the sine-wave model of Eq. (3).

upper LAXD peaks relative to that of the central peak of $\approx 18.5\%$ and 7% for the 15 Å/15 Å sample $\approx 9\%$ and 1% for the 8 Å/8 Å sample. The heights of the filled bars in Figs. 1 and 2 show that these predictions are too small in both cases. No computer fit is given for the 8 Å/8 Å data because no single pair of integer number of atoms is appropriate to the data, and combining two or more pairs requires the use of adjustable parameters for the relative proportions, which we prefer to avoid.

From these results, we conclude that the concentration profile is somewhat sharper than a sine wave in these very thin-layer samples. And even for a sine wave, the Cu-Mn and Ag concentrations in the middle of the respective Cu-Mn and Ag layers would still each be 100%. We thus conclude that, for metal-metal MS's with such thin bilayer widths, our sputtering process must be good enough to keep the two metals from spreading more than about two atomic planes ($\approx 4-5$ Å) into each other (corresponding to total bilayer widths of $\leq 8-10$ Å).

Interdiffusion: From the known bulk diffusion constants for the constituents of our MS [which have diffusion activation energies of ≈ 2 eV (Ref. 32)], bulk diffusion in defect-free material must be negligible both at room temperature and at the slightly higher temperatures reached during sputtering by the samples for which χ data are presented in this paper. Our samples, however, are not defect free. We shall show below that they have fairly small grains, and that independent resistivity measurements of sputtered pure Cu films yield residual resistivities which suggest defect concentrations in the films (including grain boundaries) of about 1%. If, to obtain an upper bound, we assume that these defects are all vacancies, then bulk diffusion could become feasible. It is thus necessary to turn to experimental data to see whether or not such diffusion is present.

To see whether bulk diffusion of Mn was occurring in our samples after preparation, we remeasured T_f and LAXD on some $Cu_{1-x}Mn_x$/Cu MS held at room temperature for times ranging from several months to more than a year. No perceptible changes were found in either quantity, indicating that no significant Mn spreading is occurring at room temperature.

We also checked whether values of T_f for samples maintained below 20 °C during sputtering—produced using a recently installed substrate cooling system[33]—agreed with those obtained in this paper for samples that had warmed up to ≈ 60 °C during sputtering. They did.

This combination of long-term stability against Mn diffusion at room temperature, with insensitivity of T_f to sputtering temperatures slightly above or below room temperature, indicates that bulk interdiffusion during and after sputtering is not significant.

In contrast to bulk diffusion, diffusion along grain boundaries during sputtering cannot be ruled out. For our $Cu_{1-x}Mn_x$/Si MS, we shall see below that the Cu-Mn grain dimensions are equal to or smaller than the Cu-Mn layers widths and that the grains terminate at the $Cu_{1-x}Mn_x$/Si interfaces. Si diffusion into the Cu-Mn along grain boundaries probably contributes significantly to the irregular boundaries in $Cu_{1-x}Mn_x$/Si MS's shown in Fig. 3, and perhaps also to more rapid decreases in T_f for $Cu_{1-x}Mn_x$/Si MS's than for $Cu_{1-x}Mn_x$/Cu MS's by isolating the Cu-Mn grains from each other due to coating of the grain surfaces with Si. For our $Cu_{1-x}Mn_x$/Cu, MS, on the other hand, the MS's with small Cu-Mn layer widths have grains much larger than those widths. While grain-boundary diffusion probably contributes to the ≤ 5 Å spreading in layer width that we estimate below for our $Cu_{1-x}Mn_x$/Cu MS, we doubt that it has any important additional effect on our data.

FIG. 3. Bright-field image of a $Cu_{0.93}Mn_{0.07}$/Si (200 Å/70 Å) MS taken on the TEM. Magnification = 190 K.

D. Structural characterization

Because of the limitations described in Sec. II B on the information that x rays give about our MS, we used several complementary techniques to independently check that our samples were layered and to structurally characterize the samples. Most of these other techniques were limited to MS's with relatively thick Cu-Mn layers.

To obtain information in real space, cross sections ≈ 500 Å thick were made for transmission electron microscope (TEM) and field emission-scanning transmission electron microscope (FE-STEM) analyses of samples with relatively wide layers. Direct imaging of the cross sections and energy-dispersive x-ray (EDX) analysis were used to ascertain the presence of layering. The electrical resistivities of the samples were measured to (i) check that the metallic layers of the narrowest layer $Cu_{1-x}Mn_x$/Si MS remained continuous; and (ii) permit

estimation of the extent to which interfacial mixing deposited impurities in the Cu-Mn layers of the $Cu_{1-x}Mn_x$/Si MS or in the Cu layers of the $Cu_{1-x}Mn_x$/Cu MS.

LAXD and selected area diffraction (SAD) measurements provided k-space information that was used to analyze the internal structure of the layers, and x rays were used to determine the average bilayer thickness d via SAXD for the $Cu_{1-x}Mn_x$/Si MS and LAXD for the $Cu_{1-x}Mn_x$/Cu MS. We examine these results in the order listed.

1. Cross sections

To analyze the structural and chemical compositions of the MS in both the TEM and the FE-STEM, a simple procedure using a Reichert-Jung Ultracut E Microtome was developed by J. Heckman at the MSU Center for Electron Optics Studies. The sample was coated with epoxy while still on the substrate. The epoxy and sample were then removed from the substrate and placed in an epoxy-filled mold. The epoxy was allowed to harden and then shaped to fit into the microtome. The microtome sliced the sample with a diamond knife edge to thicknesses ≤ 1000 Å. The slices were floated on water, picked up on Ni grids, and transferred to the microscope. If the thin films were too opaque to the electron beam, the grid was removed from the microscope and the sample further thinned in a VCR Group, Inc., Model I.306 ion-reactive gas milling system.

a. Direct imaging. Figure 3 shows a bright-field image of a $Cu_{0.93}Mn_{0.07}$/Si (200 Å/70 Å) MS taken on a JEOL JEM-100 CX II transmission electron microscope (TEM). We identify the darker and wider material as being the electronically more dense Cu-Mn. The Cu-Mn layers appears to be composed of crystallites with diameters comparable to the layer thickness; LAXD values for crystallite sizes will be given in Sec. II D 3. A good deal of structure is visible at the interfaces, along with evidence of some local deformations of the layers by the microtome. No evidence of crystallites is seen in the Si layers, consistent with our expectation that the Si layers would be amorphous.

b. Energy-dispersive x-ray analysis. EDX analysis in a VG HB501 STEM was used to obtain corroborative evidence of spatial variations in chemical composition of a (300 Å/300 Å) $Cu_{0.79}Mn_{0.21}$/Cu MS and a (70 A/70 Å) $Cu_{0.79}Mn_{0.21}$/Si MS, both of which had enough Mn to permit semiquantitative analysis of all of the MS constituents and wide enough layers so that beam spreading in the sample did not completely wash out any variations. Such beam spreading precluded the use of this technique on samples with layers much thinner than 100 Å.

The electron beam was scanned once over the entire width of the cross section perpendicular to the layers. The intensities of the core energies of each element analyzed were smoothed and plotted as a function of scanning distance. A sample line plot for the (300 Å/300 Å) $Cu_{0.79}Mn_{0.21}$/Cu MS is shown in Fig. 4. The variations in chemical composition of the elements are consistent with chemical layering; the nearly sinusoidal form of the

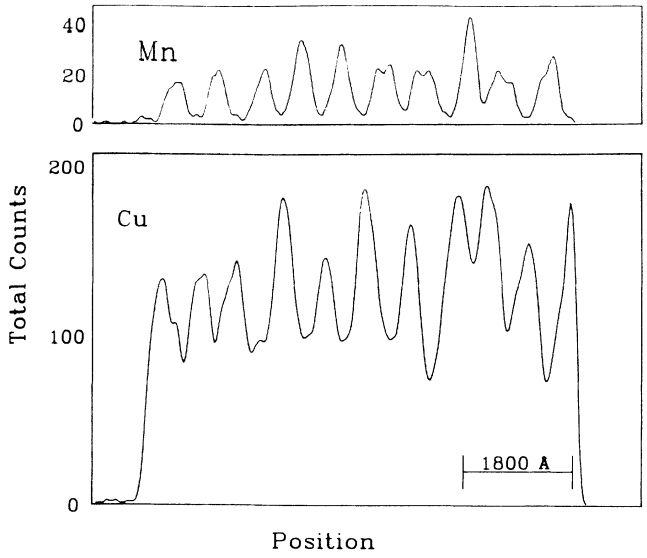

FIG. 4. Smoothed EDX scan of a $Cu_{0.79}Mn_{0.21}$/Cu (300 Å/300 Å) MS taken on the FE-STEM. Beam spreading of about 100 Å in the sample produces most or all of the sinusoidal form of the data, and spurious local structure is due primarily to smoothing of noisy data.

data is due to beam spreading in the sample, and the occasional local structure is due primarily to smoothing of noisy data. In the (70 Å/70 Å) $Cu_{0.79}Mn_{0.21}$/Si MS, beam spreading washed out most of the evidence of layering, and smoothing of the noisy data again introduced

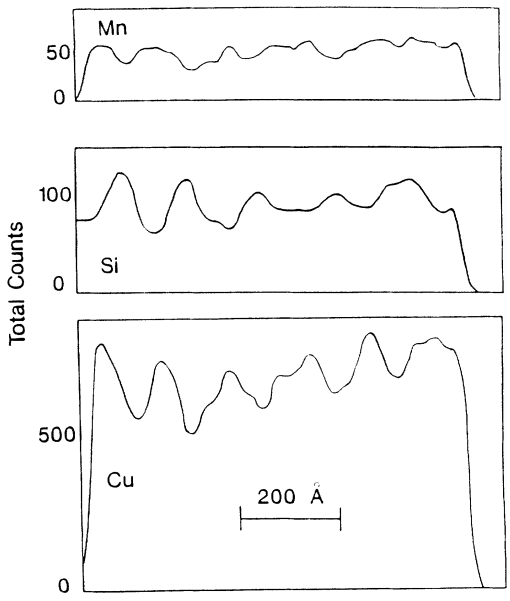

FIG. 5. Smoothed EDX scan of a $Cu_{0.79}Mn_{0.21}$/Si (70 Å/70 Å) MS taken on the FE-STEM. Beam spreading of about 100 Å in the sample has washed out most of the layering, and smoothing of noisy data has produced some spurious apparent local structure.

some spurious local structure. But the locations of the peaks and valleys in Fig. 5 are generally correlated for the Cu and Mn and anticorrelated with the Si.

2. *Resistivity measurements*

The van de Pauw[34] technique was used to measure the resistivities of all the MS's that were used for susceptibility measurements. In addition, the usual "wire" (or "bar") geometry was used for a few specially prepared samples to check that the van de Pauw results were reliable.

Measurements were made on six different types of samples: $Cu_{1-x}Mn_x$/Cu MS's on Si substrates; Cu-Mn thin films on Si and sapphire substrates; $Cu_{1-x}Mn_x$/Si MS's, with varying $W_{Cu\text{-}Mn}$, on Si and sapphire substrates; and $Cu_{1-x}Mn_x$/Si MS's, with varying W_{Si} on Si substrates.

a. $Cu_{1-x}Mn_x$/Si MS. Figure 6 shows resistivity versus inverse layer thickness for $Cu_{0.96}Mn_{0.04}$/Si MS's. Similar plots for the other three Mn concentrations are given elsewhere.[35] The MS data are shown as circles. The squares in Fig. 6 represent resistivity data for Cu-Mn thin films. Open symbols correspond to measurements made with the van de Pauw technique and solid symbols to measurements with the bar geometry. Using the value for ρ_{bulk}, obtained from 5000 Å thick samples, the dashed line in Fig. 6 is the fit to a single-film Fuchs model with completely diffuse interface scattering[36] in the limit $W_{Cu\text{-}Mn} \gg \lambda$ (where λ is the estimated bulk conduction electron mean free path). The comparison in Fig. 6 of the resistivities of the $Cu_{1-x}Mn_x$/Si MS's with those of the Cu-Mn thin films and the Fuchs model shows that there is definitely some contamination of the Cu-Mn layers by Si. Whether this involves primarily silicide formation or physical penetration is not clear. Bulk diffusion of substantial Si into the Cu-Mn should not take place even at the highest temperatures (<100 °C) reached by these samples during the sputtering process. But the data of Fig. 3 indicate that Si might penetrate along grain boundaries.

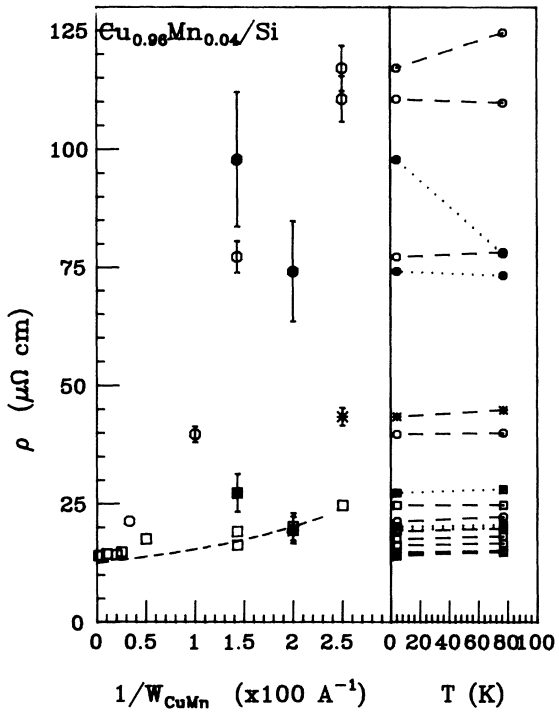

FIG. 6. ρ vs $(1/W_{Cu\text{-}Mn})$ for $Cu_{0.96}Mn_{0.04}$/Si MS. The open circles indicate MS measured with the van de Pauw technique; the solid circles indicate MS's measured with the four-probe bar technique; the open squares indicate thin films measured with the van de Pauw technique, and the solid squares indicate thin films measured with the four-probe bar technique. The dashed line is the fit to the Fuchs model. Inset on the right: ρ at 4.2 K and 77 K.

The ρ data for the $Cu_{1-x}Mn_x$/Si MS's with 21% Mn displayed much more scatter for a given Cu-Mn layer thickness than the MS's with smaller Mn concentrations,[35] and showed changes in the sign of $d\rho/dT$ which did not vary systematically with Cu-Mn layer thickness. The T_f values for these samples were also much more scattered than those for the samples with smaller Mn concentrations. We associated most of this behavior with observed macroscopic inhomogeneities in the target, and we, therefore, concentrate our analysis of $Cu_{1-x}Mn_x$/Si MS's upon samples with Mn concentrations less than 21%.

b. $Cu_{1-x}Mn_x$/CuMs. Table I compares the total resistivities (ρ_{tot}) of the $Cu_{1-x}Mn_x$/Cu ($x=0.7$) MS with three models. (1) ρ_{spec} represents parallel conduction [i.e., $(1/R_{tot})=(1/R_{Cu})+(1/R_{Cu-Mn})$] by the Cu and Cu-Mn layers assuming specular reflection from the interfaces between the Cu-Mn and Cu layers. The interfaces thus do not contribute to ρ. The values of ρ_{Cu} and $\rho_{Cu\text{-}Mn}$ used in calculating R_{Cu} and $R_{Cu\text{-}Mn}$ were determined from independent measurements on sputtered thick Cu and Cu-Mn films; although we will see below that the crystallite sizes of the MS vary with layer thickness, corrections for such changes are not large enough to materially alter the numbers in Table I. (2) ρ_{diff} represents parallel conduction by the Cu and Cu-Mn layers using the Fuchs model[36] of completely diffuse scattering at the interfaces—i.e., scattering with complete loss of knowledge of the direction of the initial electron

TABLE I. The total resistivity ρ_{tot} for the $Cu_{0.93}Mn_{0.07}$/Cu MS's, compared with a specular scattering model, a diffuse scattering model, and a uniform model for the MS's. All resistivities are in $\mu\Omega$ cm.

		$Cu_{0.93}Mn_{0.07}$/Cu			
Sample	$W_{Cu\text{-}Mn}$ (Å)	ρ_{tot}^{meas}	ρ_T^{spec}	ρ_T^{diff}	ρ_T^{un}
121-3	5000	19.0±0.8			
121-2	500	7.0±0.03	4.54	7.00	15.83
121-4	100	4.3±0.2	2.57	4.27	7.53
121-1	50	4.3±0.2	2.29	3.84	5.16
121-6	30	3.4±0.2	2.18	3.66	4.01
121-5	20	3.2±0.1	2.11	3.57	3.38

momentum. In this model, which we expect to be the the most realistic of the three described, the interfaces contribute maximally to ρ. (3) ρ_{uniform} is the resistivity expected if the Mn were distributed uniformly throughout the $Cu_{1-x}Mn_x$/Cu sample. This model thus involves no layering.

If our samples are layered, and if the "bulk" resistivities of the individual Cu and Cu-Mn layers of the MS's are approximately the same as in the test films, then the experimental ρ should fall between models (1) and (2)—probably lying closer to (2). In addition, for samples with relatively thick Cu-Mn layers, models (1) and (2) should both yield values of ρ considerably less than model (3), since ρ for Cu was much smaller than ρ for the alloys.

To within experimental uncertainties, the values of ρ_{tot} listed in Table I do lie within the limits set by ρ_{spec} and ρ_{diff}, a behavior that is consistent with layering. Similar behavior was found for most of the values of ρ_{tot} for other Mn concentrations.[35]

3. *Crystallite sizes from large-angle x-ray diffraction and selected area diffraction*

a. LAXD. Quantitative estimates of crystallite dimensions, S, perpendicular to the layers were obtained from measurements of the widths of LAXD diffraction lines in both $Cu_{1-x}Mn_x$/Si and $Cu_{1-x}Mn_x$/Cu MS, using the relation[20]

$$S = K\lambda/\beta\cos\theta \ . \tag{4}$$

Here, K is a constant approximately equal to 1, λ is the x-ray wavelength, θ is the Bragg angle, and β is the width of the peak in rad.

$Cu_{1-x}Mn_x$/Si: In $Cu_{1-x}Mn_x$/Si LMS's, we only observed LAXD reflections from the ⟨111⟩ plane of Cu-Mn, indicating strong preferential orientation of Cu-Mn crystallites in the plane perpendicular to the layers and amorphous Si layers. As the Cu-Mn layer size decreased, the intensity of the ⟨111⟩ peak decreased and its width increased. We attribute this behavior to a reduction in average crystallite size S. Table II displays the intensities and widths of the peaks as a function of Cu-Mn layer thickness, along with estimates of S. We see that the Cu-Mn crystallite sizes were typically less than or equal to the Cu-Mn layer thickness. No satellites were found in the LAXD spectra for the $Cu_{1-x}Mn_x$/Si MS's; their absence is consistent with Si layers that are amorphous and fluctuate in thickness by more than 5%.[25]

CuMn/Cu: In $Cu_{1-x}Mn_x$/Cu LMS's, we only observed LAXD reflections from the ⟨111⟩ planes of Cu-Mn and Cu (or from the ⟨111⟩ plane of the average lattice for sufficiently thin layers), again indicating strong crystallite orientation. Figure 7 contains a representative scan of a (70 Å/300 Å) $Cu_{0.86}Mn_{0.14}$/Cu MS, showing both the main Cu and Cu-Mn peaks which we discuss in this section and four weak satellite peaks that we discuss in Sec. II D 4. The peak intensities, estimated peak widths, and estimated crystallite sizes for the main peaks in the $Cu_{0.93}Mn_{0.07}$/Cu MS are contained in Table III. We see that for the thinner Cu-Mn layers, the crystallite sizes are much larger than the layer widths, suggesting that the Cu-Mn layers tended to grow locally epitaxially on the thicker Cu layers.

b. Selected area diffraction. Selected area diffraction (SAD) measurements were performed on both $Cu_{1-x}Mn_x$/Si and $Cu_{1-x}Mn_{1-x}$/Cu MS's to obtain information about crystallite orientations and sizes in the planes of the layers. This technique involves sending a parallel beam of electrons through an area $\sim 1\ \mu m^2$ of the sample.

Figure 8 shows both the SAD pattern and a line scan

TABLE II. LAXD analysis of $Cu_{0.86}Mn_{0.14}$/Si MS's. Bragg peak intensity, width, and calculated crystallite size are listed.

Sample no.	$W_{\text{Cu-Mn}}$ (Å)	$Cu_{0.86}Mn_{0.14}$/Si Intensity	Width	Size (Å)
120-1a	50	153	2.37	40
120-1b	50	175	2.28	42
120-3b	70	684	1.69	56
120-5a	100	937	1.48	64
120-5b	100	1280	1.45	65
120-4a	500	2034	0.81	150
120-4b	500	2213	0.78	150
120-2a	1000	1531	0.64	190
120-2b	1000	1258	0.70	170
120-6b	5000	3084	0.56	210

TABLE III. LAXD analysis of $Cu_{0.93}Mn_{0.07}$/Cu MS's. Bragg peak intensity, width, and calculated crystallite size are listed.

Sample no.	$W_{\text{Cu-Mn}}$ (Å)	$Cu_{0.93}Mn_{0.07}$/Cu Intensity	Width	Size (Å)
121-5b	20	99 619	0.21	440
121-6b	30	51 696	0.22	430
121-1b	50	47 498	0.27	370
121-4b	100	14 121	0.37	a
121-2b	500	4 156	0.54	a

[a]Peak composed of two unseparated peaks.

TABLE IV. Analysis of SAD lines scan for $Cu_{0.86}Mn_{0.14}$/Cu (200 Å/300 Å) MS's. The column labeled "factor" indicates the ratio $D_{\text{obs}}/D_{\text{calc}}$, which differs from unity due to the fact that the SAD system was not independently calibrated.

Line ID	$Cu_{0.86}Mn_{0.14}$/Cu (200 Å/300 Å) θ	D_{cal} (cm)	D_{obs} (cm)	Factor
(111)	0.51°	1.775	2.35	1.324
(200)	0.59°	2.050	2.69	1.312
(220)	0.83°	2.900	3.83	1.320
(311)	0.97°	3.401	4.53	1.332
(222)	1.02°	3.552	Absent	
(400)	1.17°	4.102	5.43	1.324
(331)	1.28°	4.470	6.10	1.365
(420)	1.31°	4.587	Absent	
(422)	1.44°	5.026	6.65	1.323

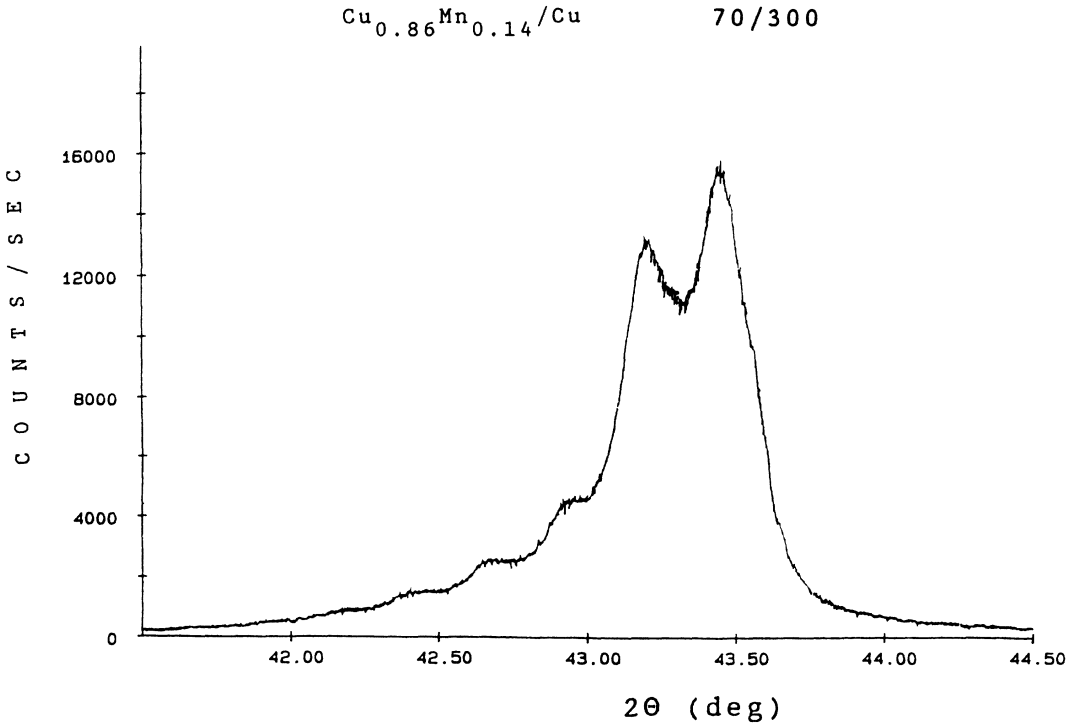

FIG. 7. LAXD scan (solid curve) of a $Cu_{0.86}Mn_{0.14}/Cu$ (70 Å/300 Å) MS.

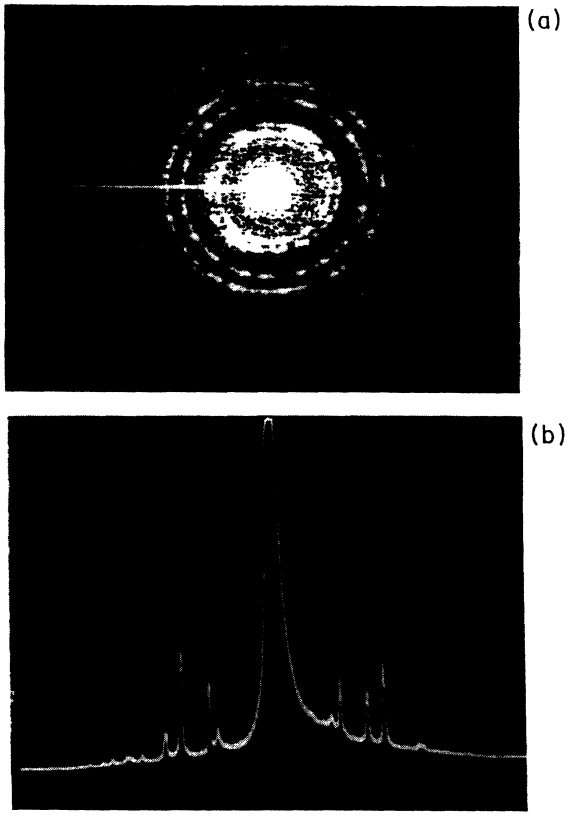

FIG. 8. (a) SAD pattern of a $Cu_{0.86}Mn_{0.14}/Cu$ (200 Å/300 Å) MS taken on the FE-STEM. (b) Line scan of the SAD pattern of (a).

through this pattern for a $Cu_{0.86}Mn_{0.14}/Cu$ (300 Å/300 Å) MS. The SAD pattern shows diffraction rings, indicating that the sample is composed of crystallites. The in-plane crystallite sizes S, which can be estimated from the structure of the image, are consistent with the sizes perpendicular to the layers obtained in Sec. II D 3 a from LAXD. The nonuniform nature of the rings indicates that there are preferred crystallite directions in the plane of the layers. The line scan is analyzed in Table IV. The observed diffraction peaks are consistent with the fcc lattice of Cu. The SAD pattern[35] of a $Cu_{0.86}Mn_{0.14}/Si$ (70 Å/70 Å) MS had broader, smoother rings than Fig. 8, indicating that the crystallite sizes were significantly smaller than in the $Cu_{1-x}Mn_x/Cu$ MS. This difference is consistent with the results obtained from LAXD described in Sec. II D 3 a. No lines attributable to crystalline Si were seen.

4. Bilayer thickness, d, and layer profiles from SAXD and LAXD measurements

a. $Cu_{1-x}Mn_x/Si$. We noted in Sec. II D 3 that only SAXD satellites were seen in $Cu_{1-x}Mn_x/Si$ MS's. These scans showed chemical layering for 100 Å $\leq d \leq$ 270 Å (i.e., 30 Å $\leq W_{Cu\text{-}Mn} \leq$ 200 Å). For larger values of d, the angles at which the SAXD peaks would have appeared were too small to resolve; for $d = 90$ Å (corresponding to $W_{Cu\text{-}Mn} = 20$ Å), no layering was seen. From the fact that layering was seen for $W_{Cu\text{-}Mn} = 30$ Å, but not for $W_{Cu\text{-}Mn} = 20$ Å, we infer that boundary spreading in the $Cu_{1-x}Mn_x/Si$ MS was between 10 and 15 Å (i.e., total boundary width $\approx$20–30 Å). Figure 9 contains SAXD

TABLE V. SAXD analysis of $Cu_{0.93}Mn_{0.07}$/Si MS's. The x-ray bilayer width $d_{x\text{-ray}}$ is compared to the width d_{sputt} calculated from the sputtering rate and sputtering time.

	$Cu_{0.93}Mn_{0.07}$/Si			
Sample no.	Layers	Peaks	d_{sputt} (Å)	$d_{x\text{-ray}}$ (Å)
30-b	60	6	100	101±5
32-b	84	6	120	119±6
56-b	60	4	120	122±6
28-b	67	4	130	134±7
55-b	43	6	140	139±7
33-b	44	9	210	210±11
24-b	31	5	170	169±8
23-b	25	10	270	277±14
55-b	15	3	270	256±13

scans for two different $Cu_{1-x}Mn_x$ (14%)/Si (70 Å/70 Å) samples, one showing a typical number of Bragg peaks (i.e., 4–9) and the other the largest number seen (i.e., 14). Table V compares the bilayer widths for $x=0.07$, estimated from (a) the measured sputtering rates and sputtering times and (b) the slope of the line found upon

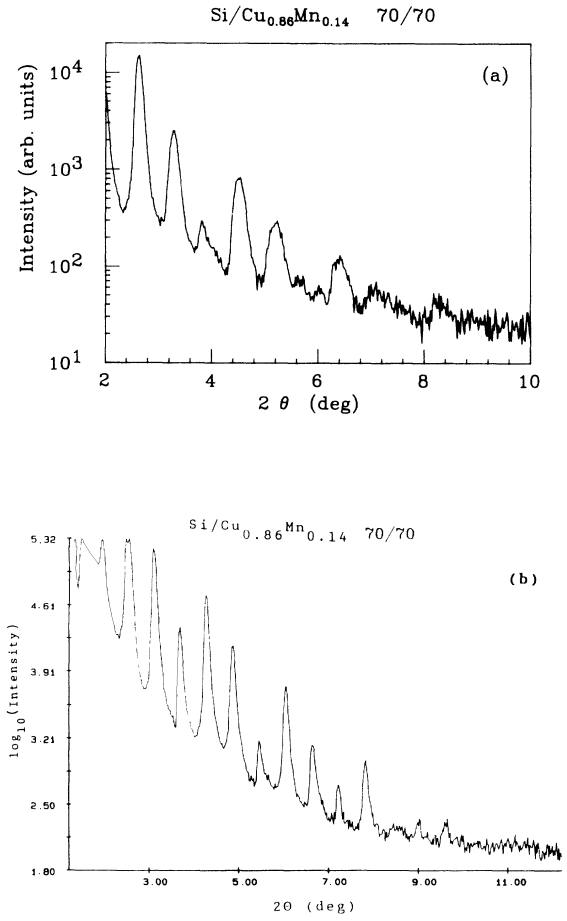

FIG. 9. SAXD scans of two different $Cu_{0.86}Mn_{0.14}$/Si (70 Å/70 Å) samples showing a typical scan (a) and an unusually good scan (b).

TABLE VI. LAXD analysis of $Cu_{0.86}Mn_{0.14}$/Cu MS's. The x-ray bilayer width $d_{x\text{-ray}}$ is compared to the width d_{sputt} calculated from the sputtering rate and sputtering time.

	$Cu_{0.86}Mn_{0.14}$/Cu			
Sample no.	$W_{Cu\text{-}Mn}$ (Å)	No. satellites	d_{sputt} (Å)	$d_{x\text{-ray}}$ (Å)
113-3b	30	6	330	351
113-6b	50	4	350	363
113-4a	70	5	370	359
113-4b	70	4	370	374
113-1a	100	6	400	398

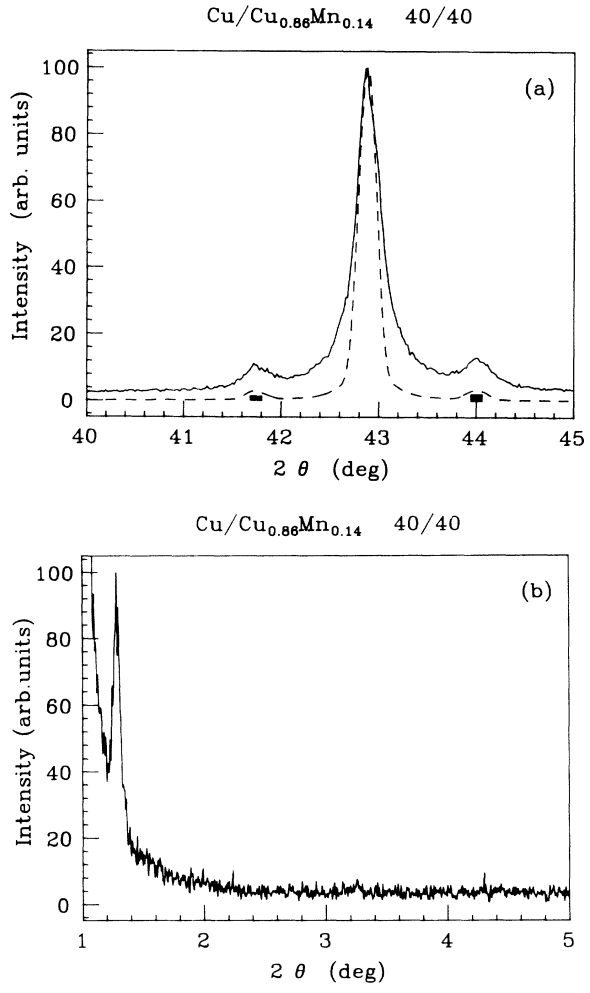

FIG. 10. Selected LAXD (a) and SAXD (b) scans from two different $Cu_{0.86}Mn_{0.14}$/Cu (40 Å/40 Å) MS's prepared together. Each scan is the better of the two choices available. (a) The dashed curve is a computer calculation for a square-wave chemical profile with 20 atoms of each constituent and coherence length ≈400 Å. The filled bars represent satellite heights predicted by the sine-wave model of Eq. (3); these are to be compared with the excess intensities of the LAXD satellite peaks above backgroumd. (b) Only the odd-order SAXD satellites should be present in a square-wave MS with equal layer widths; the third-order satellite was too small to be resolved.

plotting the angles of the SAXD peaks versus a set of assumed integer values for the orders of the peaks. These two independent estimates are typically within several percent of each other, giving us confidence in our determination of average bilayer thickness to within such an uncertainty.

b. CuMn/Cu. LAXD: Weak LAXD satellites were usually seen in $Cu_{0.86}Mn_{0.14}$/Cu MS's, and sometimes also in $Cu_{0.93}Mn_{0.07}$/Cu MS's. Figure 7 illustrates such satellites for a (70 Å/300 Å) MS. Table VI shows that the values of d determined from these LAXD satellites were generally in satisfactory agreement with the intended values.

The satellites of Fig. 7 are not only small, but are also superimposed on a large and varying background, making it impossible to use them to derive useful information about layer spreading. To obtain better information about such spreading, we consider LAXD measurements on MS's that we have prepared for other studies, that have either relatively small values of both $W_{Cu\text{-}Mn}$ and W_{Cu}, or larger but equal values. Such MS's eliminate the problem of large and varying background.

We start with LAXD data for a $Cu_{0.86}Mn_{0.14}$/Cu (40 Å/40 Å) MS [Fig. 10(a)] which can be compared both with a computer calculation for a square-wave profile with 20 atoms each of Cu and $Cu_{0.86}Mn_{0.14}$ (dashed curve) and with Eq. (3) (solid bars). Taking into account background effects, the square-wave profile gives a reasonable fit, but the predictions of Eq. (3) are too small. LAXD satellites for MS's with still narrower Cu layers are shown in Figs. 11(a) and 12(a). From the persistence of satellites in Fig. 12(a) for Cu layers as thin as 10 Å, we infer that penetration of Mn into the Cu interlayers of $Cu_{1-x}Mn_x$/Cu MS's with $d \leq 50$ Å must be limited to ≤ 5 Å, in agreement with the conclusions reached in Sec. II C 2 b for interpenetration of Ag and Cu. The data of Figs. 11(a) and 12(a) are compatible with similar con-

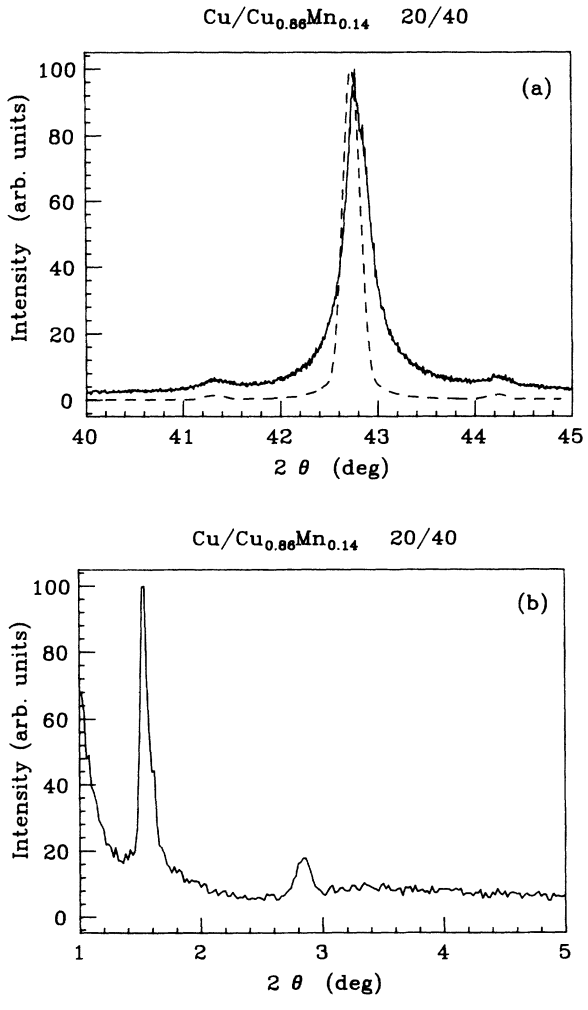

FIG. 11. LAXD (a) and SAXD (b) scans of a $Cu_{0.86}Mn_{0.14}$/Cu (40 Å/20 Å) MS. The second-order SAXD satellite is visible in this MS with unequal layer widths. The dashed curve is a computer calculation assuming a square-wave chemical profile and coherence length ≈400 Å.

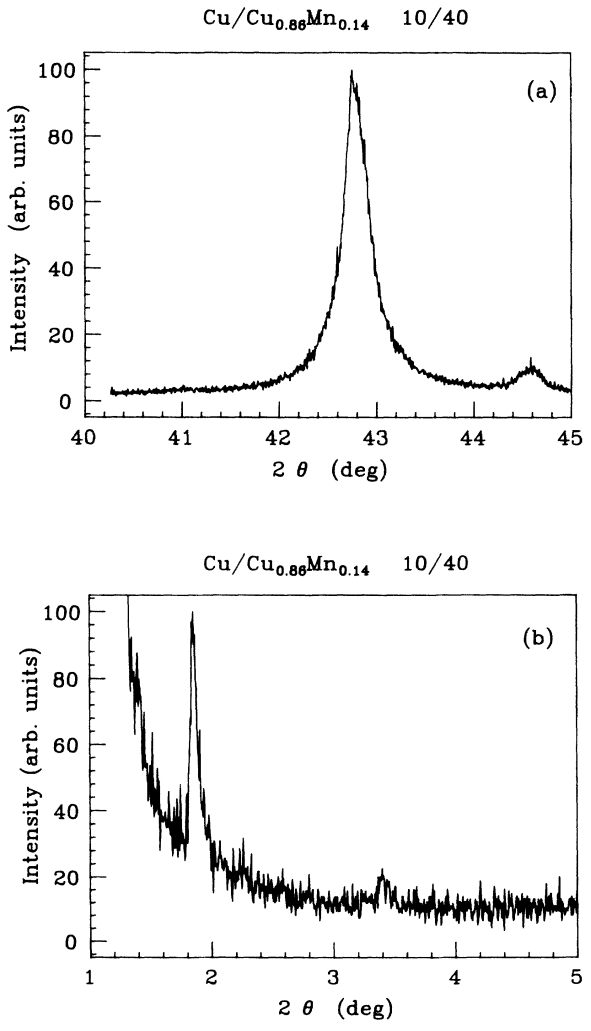

FIG. 12. LAXD (a) and SAXD (b) scans of a $Cu_{0.86}Mn_{0.14}$/Cu (40 Å/10 Å) MS. As in Fig. 11, the second-order SAXD satellite is visible.

clusions for d up to ≈ 80 Å.

If we knew that layer spreading in our MS was independent of d, we could conclude from the data just presented that the layer spreading in $Cu_{1-x}Mn_x$/Cu MS's with values of $d \gg 50$ Å is also ≤ 5 Å. However, it was recently reported[19] that layer spreading in evaporated Co/Cr MS's increased from <5 Å for $d=20$ Å, to ≈ 8 Å for $d=50$ Å, and then to ≈ 10 Å for $d=80$ Å, at which value it appeared to level off. We must therefore consider the possibility that layer spreading might also increase with increasing d in our MS.

To set upper bounds on layer spreading in samples with $d \gg 50$ Å, we examined the LAXD satellite intensities of MS's with equal layer widths of $Cu_{0.96}Mn_{0.04}$ and $Cu_{0.86}Mn_{0.14}$, and $d=140$, 200, and 400 Å. The data are shown in Fig. 13, along with (a) computer-generated predictions (dashed curves) for square-wave profiles for fixed numbers of atoms in each layer, and (b) predictions from Eq. (3) for sine-wave profiles. The satellites agree reasonably well with the square-wave predictions and are noticeably larger than the sine-wave predictions. The data thus do not require that we invoke any layer spreading greater than the ≈ 5 Å derived above.

We considered, and rejected, the possibility of undertaking more complex analysis of the data of Fig. 13 (using, e.g., trapezoidal profiles), on the basis that the differences between the square-wave and sine-wave predictions were too small to permit reliable determinations of the adjustable parameters that would have to be introduced. Rather, we limit ourselves to asking what absolute bounds we can set from these data. Conservatively, we can say that any layer spreading must be much less than $d/4$, since a spreading of $d/4$ would approximate a sine-wave profile. That is, the layer spreadings for $d=140$, 200, and 400 Å must be $\ll 35$ Å, $\ll 50$ Å, and $\ll 100$ Å, respectively. Unfortunately, these bounds are so much larger than 5 Å that the condition "much less than" does not eliminate the possibility of additional layer spreading. We note, however, that the layer spreading of ≤ 5 Å that we find for $d=50$ Å in our $Cu_{1-x}Mn_x$/Cu MS is less than the ≈ 8 Å found for $d=150$ Å in Co/Cr. It thus seems likely that our layer spreading for $d \geq 100$ Å will also be smaller than the 10 Å found for Co/Cr.

SAXD: As indicated in Sec. II B, we did not see any SAXD satellites in $Cu_{1-x}Mn_x$/Cu samples with $d > 300$ Å. We were, however, able to see weak SAXD satellites [Figs. 10(b), 11(b), and 12(b)] in test samples with smaller values of d. The values of d derived from these peaks agreed with those from the LAXD measurements to within mutual uncertainties. The presence of these peaks provides further evidence of chemical layering in these samples; in particular, the observation of a second-order peak in the (40 Å/10 Å) MS supports our claim that penetration of Mn into the Cu interlayers of $Cu_{1-x}Mn_x$/Cu MS's did not take place over a distance of more than about 5 Å.

5. *Summary and conclusions concerning sample properties*

The data presented above indicate that the Cu-Mn SG layers in all of our MS's were crystalline with strong (111)

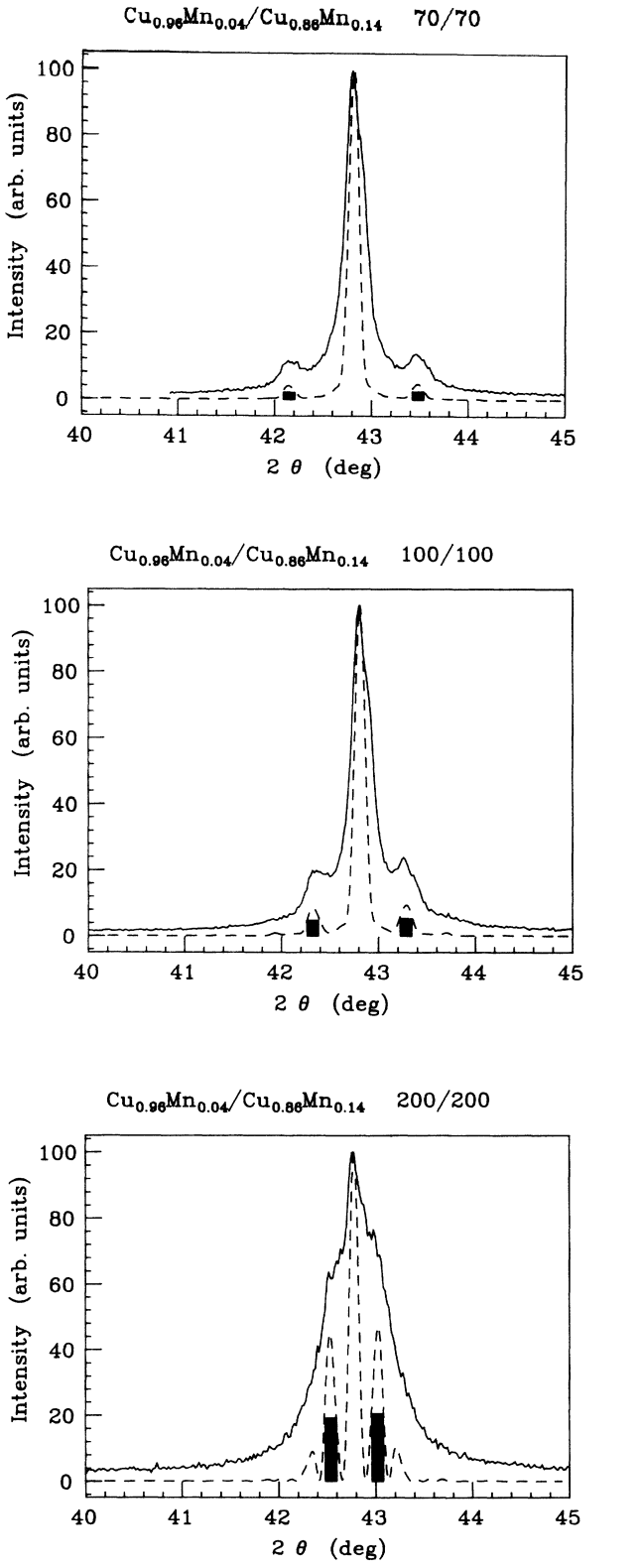

FIG. 13. LAXD scans of $Cu_{0.96}Mn_{0.04}/Cu_{0.86}Mn_{0.14}$ (70 Å/70 Å), (100 Å/100 Å), and (200 Å/200 Å) MS's. The dashed curves represent computer calculations assuming a square-wave chemical profile and coherence length ≈ 400 Å. The filled bars indicate satellite heights predicted by the sine-wave model of Eq. (3); these are to be compared with the excess intensities of the satellite peaks above background.

texture along the axis perpendicular to the layers. The Cu layers in $Cu_{1-x}Mn_x$/Cu MS's were also crystalline with strong (111) texture along the axis perpendicular to the layers, and the crystallites in these MS's had dimensions ≥ 400 Å, so that they generally extended over more than one bilayer in MS's with thin Cu-Mn layers. In the $Cu_{1-x}Mn_x$/Si MS's, the Si layers were amorphous and the crystallite sizes in the Cu-Mn layers tended to be smaller than the Cu-Mn layer widths.

Layering satellites were seen in $Cu_{1-x}Mn_x$/Si MS's down to individual layer widths ≤ 30 Å, but not for layers of 20 Å. We thus conclude that the layer spreading in these MS's is most probably between 10 and 15 Å.

For the $Cu_{1-x}Mn_x$/Cu MS's, layering satellites were observed down to 10 Å on test samples with bilayer thicknesses $\leq d = 50$ Å. We thus conclude that layer spreading in such MS's is ≤ 5 Å. Tests of whether layer spreading could increase with increasing d yielded no evidence for such an increase, but the data were not good enough to completely rule it out. In the absence of evidence to the contrary, we will analyze our $Cu_{1-x}Mn_x$/Cu data assuming a layer spreading ≤ 5 Å.

III. THEORY

The theory of the behavior of SG's is still in a state of development, with as yet no agreement concerning the detailed nature of either the ground state or the elementary excitations. It is thus not possible to compare our data with a generally accepted theory, and it is necessary to examine alternative possible explanations. We limit ourselves to discussing the specific models that we investigated.

To be sure that our data are associated with fundamental size effects such as finite-size scaling, we must rule out the possibility that they are due to more trivial complicating effects such as (i) reduction in the number of nearest Mn neighbors at the surfaces of finite thickness layers; (ii) "spreading" of Mn out of the Cu-Mn layers and into the Cu or Si layers during sputtering; or (iii) contamination from the interlayer Si in our $Cu_{1-x}Mn_x$/Si MS's. We consider the first two alternatives quantitatively in this section, and the third alternative qualitatively in Sec. IV.

We then consider in detail two alternative models for how the SG transition temperature T_f^L for a sample having one finite dimension of length L should vary: (1) finite-size scaling in a system with a traditional phase transition and (2) the droplet excitation model of Fisher and Huse[2] applied to a SG for which the d_l lies between 3 and 2.

Finally, we briefly consider the finite correlation length spin-density wave (SDW) picture of Werner and coworkers.[37]

A. Complicating effects

1. *Reduction in the average number of nearest neighbors due to finite-layer thickness*

To estimate the change in behavior of an average impurity when it has fewer neighbors with which to interact, we use a model developed by Larsen,[38] called the quenched uniform model, in which T_f is related to an average over the interaction energies of the interacting impurities. This model is tractable and satisfactorily explains experimental data by Vier and Schultz[39] in ternary alloys. We shall see it predicts effects much too small to explain the behavior we observe.

In Cu-Mn, the dominant coupling between the Mn impurity atoms that determine the SG magnetic properties is expected to be the Ruderman-Kittel-Kasuya-Yosida (RKKY) interaction,[3] a spin-spin interaction mediated by the conduction electrons which is both oscillatory and long ranged [i.e., it decays asymptotically as $(R_{ij})^{-3}$, where R_{ij} is the separation between magnetic impurities]. Thus, if the thickness of a sample is reduced to a value comparable to the sample lattice parameter, impurities near the sample surface will have fewer impurity neighbors with which to interact, and the energy of the system will be reduced. This reduction in energy leads to a reduction in T_f. According to Larsen,[38] T_f can be written in terms of a sum over the RKKY interaction,

$$T_f \propto \Delta_i \propto \left[\sum_{j \neq i} [J(R_{ij})^2] \right]^{1/2} , \tag{5}$$

where Δ_i is the local energy scale of individual spins in the SG, which has the form of a root-mean-squared sum over the RKKY interaction between spin sites.

This sum can be modified to approximate a uniform environment by replacing the sum with an integral. For the RKKY interaction and the quenched-uniform model, Δ then has the form[38]

$$\Delta_i \propto \left[\frac{3J_0^2 x}{r_0^3} \int_{\xi}^{\infty} R^2 \left[\frac{r_0}{R} \right]^6 dR \right]^{1/2} , \tag{6}$$

where x is the fractional impurity concentration, r_0 is an atomic radius, and ξ is the mean distance to the nearest impurity.

Applying the quenched-uniform model to our layered geometry requires some modifications to Eq. (6). The layered geometry has cylindrical symmetry which can be used to simplify the derivation. We want the volume of a single magnetic impurity to remain the same as in the spherical system. We therefore replace the sphere by a cylinder of the same volume which at the same time minimizes the surface area. This occurs when the radius of the cylinder is equal to half its height h, so that

$$a(x) = \frac{h(x)}{2} = h_0 = r_0/(8\pi x)^{1/3} , \tag{7}$$

where r_0 is the fcc lattice parameter.

In this geometry, all impurity sites in a layer are not equivalent. The atoms near the edge of the layer do not have the same number of near-neighbor impurity atoms as those near the center of the layer. An average must, therefore, be taken over all possible lattice sites, so that Eq. (6) becomes

$$\Delta_i \propto \left\{ \frac{x\rho}{N} \sum_{i=0}^{N} \left\{ \left[\int_{a(x)}^{\infty} \int_{d_i-h_0}^{d_i+h_0} J^2(r,z)dz\, r\, dr + \int_0^{\infty} \left[\int_{d_i+h_0}^{W_{SG}/2} J^2(r,z)dz + \int_{d_i-h_0}^{-W_{SG}/2} J^2(r,z)dz \right] r\, dr \right]_{\text{impurity layer}} \right.$$
$$\left. + \left[\sum_{j=-\infty}^{\infty} \int_0^{\infty} \int_{W_{SG}/2+jW_I-d_i}^{3W_{SG}/2+jW_I-d_i} J^2(r,z)dz\, r\, dr \right]_{\text{all other layers}} \right\} \Bigg]^{1/2} , \tag{8}$$

where ρ is the density of lattice sites, W_{SG} the SG layer thickness, W_I the interlayer thickness, d_i the distance from the center of the layer to the middle of the cylinder, $J(r,z)$ the RKKY interaction, and "impurity layer" means the layer containing the impurity of interest.

Above T_0, the temperature that corresponds to the energy Δ_i, thermal fluctuations dominate and the spins look paramagnetic. Below T_0, the RKKY interaction dominates and the spins are "frozen." The SG transition temperature is, therefore, defined as $T_f = T_0 = A_0\Delta_i$, where A_0 is a proportionality constant found by equating the Δ_i bulk to the bulk experimental value of T_f. We note that this model assumes perfect boundaries and does not account for possible distortions of the Fermi energy in the $Cu_{1-x}Mn_x$/Si MS due to finite Cu-Mn film size. We will see in Sec. IV that Eq. (8) predicts a decrease in T_f with decreasing $W_{Cu\text{-}Mn}$ that is very much smaller than we actually observe.

2. *Mn "spreading" into the interlayers*

We know that our sputtering rate control is not precise enough to produce perfect $Cu_{1-x}Mn_x$/Cu or $Cu_{1-x}Mn_x$/Si interfaces. In Sec. II we estimated, from observations of x-ray satellites, that the spreading, W_s, of Mn out of the Cu-Mn layers into the Cu or Si layers was limited to less than 5 Å or 15 Å, respectively, corresponding to total interface widths of ≤ 10 Å for the $Cu_{1-x}Mn_x$/Cu MS and 20–30 Å for the $Cu_{1-x}Mn_x$/Si MS. We now wish to estimate the effects that such finite widths could have on our data.

We assume that the intended width of the SG, $W_{Cu\text{-}Mn}$, is broadened due to spreading of Mn into the interlayer region, and that the interactions between neighboring spins are strong enough that we can treat the actual spatially varying Mn concentration as an equivalent constant reduced Mn concentration, x_r, spread over a distance $W_{Cu\text{-}Mn}+2W_s$, where W_s is chosen so that the total amount of Mn is conserved. x_r is then

$$x_r = x[W_{Cu\text{-}Mn}/(W_{Cu\text{-}Mn}+2W_s)] . \tag{9}$$

For bulk $Cu_{1-x}Mn_x$ in our concentration range of x, the bulk spin-freezing temperature T_f^b is given to good approximation[8] by

$$T_f^b = T^0 c^{2/3} , \tag{10}$$

where $c = 100x$ and $T^0 \approx 10$ K is a constant. Combining Eq. (9) and (10), we can define a $T_f^{\text{eff}}(W_{Cu\text{-}Mn})$ as

$$T_f^{\text{eff}}(W_{Cu\text{-}Mn}) = T^0\{c[W_{Cu\text{-}Mn}/(W_{Cu\text{-}Mn}+2W_s)]\}^{2/3}$$
$$= T_f^b[W_{Cu\text{-}Mn}/(W_{Cu\text{-}Mn}+2W_s)]^{2/3} . \tag{11}$$

In Sec. IV we will use Eq. (11) to estimate $T_f^{\text{eff}}(W_{Cu\text{-}Mn})$ for various assumed values of W_s in $Cu_{1-x}Mn_x$/Cu and $Cu_{1-x}Mn_x$/Si MS's.

B. Phase transitions, scaling theory, and finite-size scaling

The essence of a thermodynamic phase transition is nonanalytic behavior in the free energy, which leads to divergences in physical quantities such as the specific heat and magnetic susceptibility. The leading order of this nonanalytic behavior manifests itself in the algebraic form $(T-T_c)^m$, where T_c is the critical temperature and m is called the critical exponent. It has been found experimentally that many different systems have the same critical exponents.[1] Systems with the same critical exponents are said to belong to the same "universality class," and their exponents are said to be "universal" within this class.[1]

The nonanalytic behavior at T_c results from the growth of correlations among the spins as T_c is approached. The spatial extent of these correlations is characterized by a correlation length ξ which diverges as[1]

$$\xi \sim (T-T_c)^{-\nu} . \tag{12}$$

Equation (12) defines the critical exponent ν, which can be measured in a variety of ways.[1]

Strictly speaking, a thermodynamic phase transition with its associated singularities occurs only in the limit that both the volume V and the number of particles N approach infinity while the density N/V remains constant. The thermodynamic limit is never reached in real samples, so the growth of the correlations is limited by the finite size of the sample, which thus limits the divergent behavior at the phase transition. If the curve of specific heat or magnetic susceptibility in a sample with one finite dimension L could be followed with perfect resolution, one would find that the "divergence" only grows to a finite height because the spatial extent of the correlations is limited to the sample size. In addition, the temperature T_f at which the maximum occurs is not located exactly at T_c.

Finite-size scaling theory is a phenomenological theory that addresses the behavior of experimental data for systems of finite size in the vicinity of phase transitions. It starts with the following fundamental scaling ansatz: "In the vicinity of T_c, the behavior of a system with at least one large but finite dimension L is determined by the scaled variable $y = L/\xi(t)$,"[1] where t is the reduced temperature $t = (T-T_c)/T_c$. For our samples, $L = W_{SG}$, the width of the individual SG layers.

As W_{SG} becomes smaller, the difference between $T_f(W_{SG})$ and T_c is assumed to diverge as[1]

$$\frac{T_c - T_f(t_m)}{T_c} \propto \left[\frac{W_{SG}}{\xi} \right]^{-\lambda} . \quad (13)$$

The scaling ansatz given above requires[1] that

$$\lambda = 1/\nu . \quad (14)$$

We noted in the Introduction that the structures of both the ground state and the excitations of SG's are still fundamentally unknown, and this is also true for both the order parameter and the correlation length.[3] It is thus not absolutely clear that Eqs. (13) and (14) should apply to SG's, but they have the advantage that their form is independent of the detailed nature of any of these quantities. Our intent is to compare these equations with our experimental data without any additional assumptions, and to see what conclusions result.

In addition to a decrease in T_f, finite-size scaling theory also predicts[1] an increased broadening of the phase transition with decreasing W_{SG}. We will examine this prediction also.

C. Droplet excitation model

Recently, Fisher and Huse[2] developed and applied a droplet excitation model of scaling behavior to SG's. This model starts with the assumption of an infinite lattice in a two-fold degenerate ordered SG ground state at $T=0$ K with the magnetic impurities located randomly on the lattice. The d_l of the SG is taken to be $2 \leq d_l \leq 3$. Lengths L and times t are unitless quantities, measured in terms of a characteristic microscopic length (e.g., the lattice parameter) and a microscopic time. Excitations of the system are assumed to occur by coherent flipping of all the spins in a "droplet" having a volume defined by the length scale L. When the spins are flipped, the droplet acquires a free energy which scales as

$$F \propto YL^{\Theta} . \quad (15)$$

For $d=2<d_l$, Θ_2 is negative and large-scale fluctuations with very small energies destroy the ordered SG state at any finite temperature. For $d=3>d_l$, $\Theta_3>0$ and an ordered state prevails up to a bulk SG transition temperature T_c in a sufficiently large sample. Numerical subscripts on symbols are used to indicate dimensionality.

The typical activation barrier for relaxation of low-lying droplet excitations of size $L \leq \xi$, (the correlation length) is assumed to be of height

$$B_L \propto L^{\psi} . \quad (16)$$

The relaxation time τ of a droplet of size L is then given by the inverse of the Boltzmann factor, $\tau \propto \exp(B_L/T)$, or

$$\ln\tau \propto B_L/T . \quad (17)$$

Above d_l, it is assumed that a true phase transition occurs at T_c. The bulk correlation length ξ diverges as

$$\xi \propto (T - T_c)^{\nu_3} , \quad (18)$$

both above and below T_c, where ν_3 represents the 3D value for the standard exponent[1] for the divergence of ξ. The dc limit of the nonlinear susceptibility,

$$\chi_3 = d^3M/dH^3 , \quad (19)$$

where M is the magnetization and H the applied field, also diverges as a power of $1/(T-T_c)$. The dc limit χ_{dc} of the linear susceptibility $\chi = dM/dH$ does not diverge, but displays a cusp at T_c.

Below d_l, there is no phase transition at thermodynamic equilibrium. ξ now diverges as

$$\xi \propto (Y/T)^{\nu_2} \quad (20)$$

and χ_{dc} takes on the Curie form,[2]

$$\chi_{dc} \propto C/T . \quad (21)$$

If χ is measured with a finite measuring time t_m on a sample of finite width W_{SG}, then the system does not remain in thermodynamic equilibrium down to $T=0$ K. Rather, the sample falls out of equilibrium when the correlation length reaches the film thickness. The temperature at which the departure from equilibrium occurs is called the "spin-freezing" temperature, $T_f(t_m)$.

In the current measurements, the measuring time per data point is a few minutes. We shall designate the quantity measured as $\chi_{Cu\text{-}Mn}$, and refer to it as the "dc" susceptibility, using the quotation marks to indicate that the measuring time is long, but finite. The resulting "quasi-static" T_f will be defined as the maximum in the peak in $\chi_{Cu\text{-}Mn}$.

For T near or slightly below T_c, Fisher and Huse find[2] that the combination of Eqs. (13) and (14) is modified by only a logarithmic correction,

$$\frac{T_c - T_f(t_m)}{T_c} \propto W_{SG}^{-(1/\nu_3)} \left[\ln \left[\frac{t_m}{W^{z_3}} \right] \right]^{[(\psi_3+\nu_2\psi_3)\nu_3]^{-1}} , \quad (22)$$

where z_3 is the standard exponent[1] for dynamic critical scaling. We will see that our data are not accurate enough to distinguish between Eqs. (13) and (22).

For $T \ll T_c$, the thinner the sample becomes, the further down the Curie curve it moves before the relaxation time of droplets having $L = W_{SG}$ becomes comparable to the measuring time and the sample falls out of equilibrium. Here, Fisher and Huse find an algebraic relation between $T_f(t_m)$ and W_{SG}

$$T_f/T_f^b \propto \left[\frac{W_{SG}^{\psi_3+\nu_2\Theta_3}}{\ln t_m} \right]^{(1+\nu_2\psi_2)^{-1}} . \quad (23)$$

We will compare our data for small W_{Cu-Mn} with Eq. (23).

D. The possibility of a finite-correlation-length spin-density-wave (SDW) state in Cu-Mn

Werner and colleagues[37] have reported the observation of broad satellite peaks in neutron scattering from single-crystal Cu-Mn samples. They interpreted these

peaks as indicating that Cu-Mn is not a traditional SG, but rather contains SDW's with a finite correlation length of about 40 A. If this interpretation is correct, and if such SDW's determine the behavior of our highly disordered samples, then we must consider them in interpreting our data. Since there are no published predictions for what effects finite sample size should have on such SDW's, we speculate as follows. Assuming that the derived value of 40 Å is the only correlation length in the system, we would expect no significant change in T_f until $W_{\text{Cu-Mn}}$ decreased to about 40 Å. As the SG layers became thinner than 40 Å, we would expect those SDW's that were oriented normal (or nearly normal) to the thin-film surface to be disrupted, producing a rapid falloff of T_f.

IV. DATA AND ANALYSIS

In the preceding sections of this paper we have described the structural characterization of our layered samples and the theories with which we wish to compare our data. The first part of this section contains a brief description of how the magnetic susceptibility χ of our SG samples was measured as a function of temperature, followed by detailed presentation of the χ versus temperature data for SG MS's of $Cu_{1-x}Mn_x$/Si and $Cu_{1-x}Mn_x$/Cu with $x=0.04$, 0.07, 0.14 (and 0.21 for the $Cu_{1-x}Mn_x$/Si MS). We show that zero-field-cooled data for all of our samples continue to display SG peaks in χ down to SG layer thicknesses as small as 20 Å. We show that 70 Å of Si or 300 Å of Cu magnetically decouples the SG layers. We then examine in detail how T_f decreases as the SG layer thickness decreases in both $Cu_{1-x}Mn_x$/Cu and $Cu_{1-x}Mn_x$/Si SG's, and find that T_f decreases somewhat more rapidly in the $Cu_{1-x}Mn_x$/Si SG than in the $Cu_{1-x}Mn_x$/Cu.

The second part of this section is a comparison of the χ data with the models described in Sec. III. We first use the simple quenched-uniform model to show that the observed decreases in T_f with decreasing $W_{\text{Cu-Mn}}$ are much too large to be understood simply in terms of reduction in the average number of impurity nearest neighbors. We then examine the model of Mn spreading from the Cu-Mn layers into the Cu or Si layers, and find that the observed decreases in T_f are too large to be understood in terms of our best estimates of the amounts of spreading in the $Cu_{1-x}Mn_x$/Cu ($\lesssim 5$ A) and $Cu_{1-x}Mn_x$/Si (10–15 A) MS's. A qualitative analysis of the effects of Si diffusion on resistivity, the height of the peak in the susceptibility, and the shift in T_f with $W_{\text{Cu-Mn}}$ in the $Cu_{1-x}Mn_x$/Si MS's is given, and we attribute the differences between the $Cu_{1-x}Mn_x$/Cu and $Cu_{1-x}Mn_x$/Si data to a combination of Si penetration into the Cu-Mn along grain boundaries and the additional spreading of Cu-Mn estimated for the $Cu_{1-x}Mn_x$/Si MS's. We conclude that the $Cu_{1-x}Mn_x$/Cu data are the more reliable for comparison with theories of finite-size effects in SG's. We first examine the $Cu_{1-x}Mn_x$/Cu data for T_f near T_f^b in terms of finite-size scaling analysis, and then compare the data for $T_f < T_f^b$ with predictions of the droplet excitation model of Fisher and Huse.[2] We conclude with a brief consideration of the SDW-based model of Werner *et al.*

A. Magnetic measurements

χ versus temperature measurements were made on a commercial S. H. E. Corp. V. T. S. 800 series superconducting quantum interference device (SQUID) susceptometer. This machine is capable of measuring sample magnetic moments over a wide range of temperatures and magnetic fields with a resolution of 1×10^{-7} emu.

To measure χ for our layered samples, the sample plus substrate was cut into 0.3×1 cm^2 strips to fit into the measuring coils. The magnetic field was set to zero and the sample was lowered into the space between the measuring coils, which was normally at a temperature of about 5 K (or 2 K for low-temperature measurements). The magnetic field was then raised to the measuring value of 100 or 200 G, and χ measurements were taken at a series of increasing temperatures up to 100 K. Test measurements made at 20 G indicate no significant difference in T_f. The resulting data are called the zero-field-cooled (ZFC) data. Measurements were then taken at a series of decreasing temperatures back down to 5 K (or 2 K), and the resulting data are called the field-cooled (FC) data.

Examples of determinations of the spin-freezing temperature T_f in bulk Cu-Mn from ZFC and FC dc χ measurements are given in Nagata *et al.*[40] Here dc refers to χ measurements made on time scales ≥ 1 sec. In most magnetic systems, measurements on time scales ≥ 1 sec would correspond to equilibrium measurements but, as noted in Sec. I, this is not the case for a SG.[3]

Figure 14 shows sample plots of the ZFC and FC data for several of the $Cu_{0.86}Mn_{0.14}$/Cu MS's. These curves are representative of the susceptibility data of all of

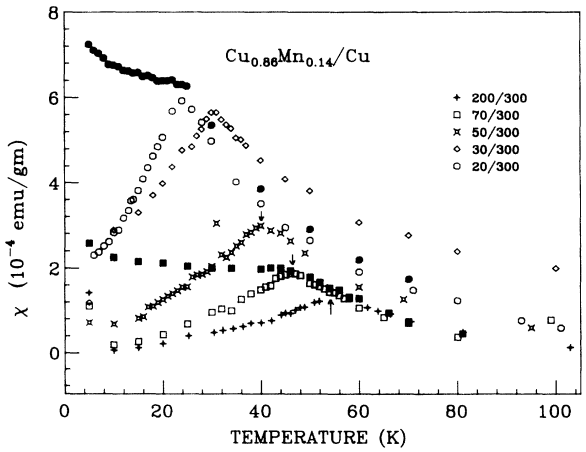

FIG. 14. χ vs T for the $Cu_{0.86}Mn_{0.14}$/Cu MS's. Open symbols indicate zero-field-cooled (ZFC) data and solid symbols indicate field-cooled (FC) data. The arrows indicate the transition temperatures.

$Cu_{1-x}Mn_x$/Cu and $Cu_{1-x}Mn_x$/Si MS's. We define the maximum of each ZFC peak as the quasistatic freezing temperature T_f. The rounded peaks produce a measuring uncertainty in T_f of $\simeq \pm 1$ K.

Starting from $T \approx 2-5$ K, the ZFC susceptibility increases with increasing temperature up to T_f with occasional anomalous jumps. We attribute these anomalous jumps to time-dependent effects (caused by somewhat different measuring times per temperature point) as χ tries to approach the (nominally) equilibrium FC susceptibility[3] in the regime where the relaxation time approximates our measuring time. Above T_f, the ZFC χ exhibits approximately Curie-like behavior.

Above T_f, the FC χ is also Curie-like, but typically appears to be slightly larger than the ZFC χ at the same temperature. In bulk spin-glass materials, the FC χ below T_f is practically constant.[3,40] In our samples we generally observe that the FC χ first decreases slightly as T is reduced below T_f and then increases as $T \rightarrow 0$ K. We do not attribute this rise in the FC data at very low temperatures to a small number of free magnetic impurities in the MS, since no similar behavior is seen in the ZFC data. We currently have no satisfactory explanation for this behavior.

Taken at face value, the data of Fig. 14 seem to show a narrowing of the peak in χ as $W_{\text{Cu-Mn}}$ decreases, which is contrary to the predictions of finite-size scaling. A careful analysis of this behavior should involve data which have been normalized to the T_f for each sample. Figure 15 shows the ZFC data of Fig. 14 thus normalized. We see that the widths of the normalized ZFC χ curves are essentially the same.

For the $Cu_{1-x}Mn_x$/Cu MS's, the absolute values of the FC susceptibility for $T > T_f$ all appear to follow generally similar Curie behavior, corresponding to approximately the same number of paramagnetic moments. This is what we would expect, since we have attempted to keep the total amount of SG material about the same in all of the samples. The residual differences in χ may be due to differences in susceptibility of the individual Si substrates backing the samples, which have much more mass than the samples. These substrates are diamagnetic and have an approximately constant susceptibility of -1×10^{-7} emu/g.

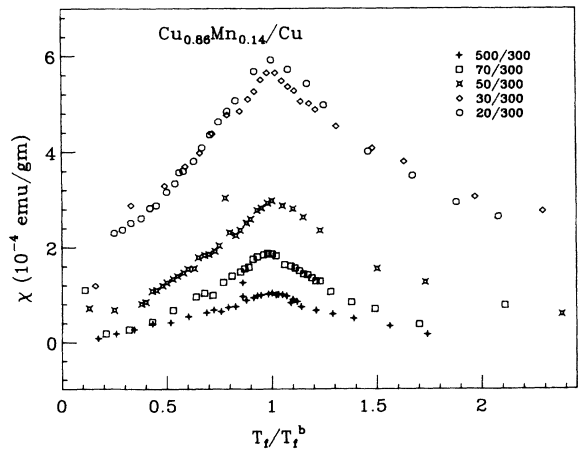

FIG. 15. χ vs (T/T_f) for the $Cu_{0.86}Mn_{0.14}$/Cu MS's.

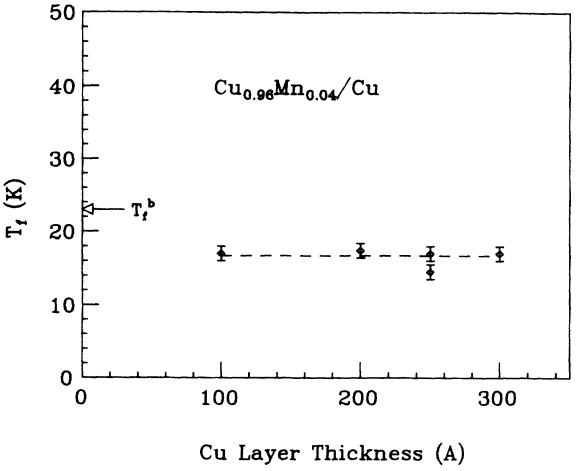

FIG. 16. T_f (for fixed $W_{\text{Cu-Mn}}$) vs W_{Cu} for $Cu_{0.96}Mn_{0.04}$/Cu MS's.

For the $Cu_{1-x}Mn_x$/Si MS's, in contrast, the absolute values of χ varied noticeably,[35] and did not appear to correlate with the Cu-Mn layer thickness. We do not yet understand this behavior, but presume that it must involve the formation of silicides at the boundary between the Si and the Cu-Mn. To determine what interlayer thicknesses of Cu and Si were large enough to magnetically decouple the SG layers from each other, samples with varying interlayer thicknesses were made.

Figure 16 shows T_f versus interlayer thickness W_{Cu} for a fixed $W_{\text{Cu-Mn}} = 100$ Å in the $Cu_{0.96}Mn_{0.04}$/Cu MS's. It is observed that no significant deviation from the tran-

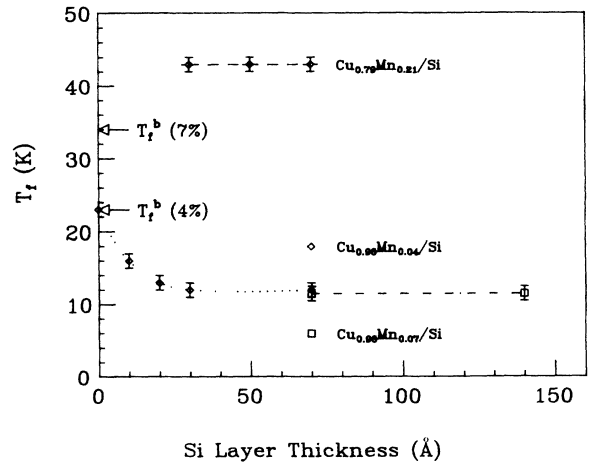

FIG. 17. T_f (for fixed $W_{\text{Cu-Mn}}$) vs W_{Si} for $Cu_{0.96}Mn_{0.04}$/Si $Cu_{0.93}Mn_{0.07}$/Si, and $Cu_{0.86}Mn_{0.14}$/Si MS's. For the MS's with 0.04 and 0.07 Mn, different SG thicknesses, $W_{\text{Cu-Mn}}$, happened to yield values of T_f that nearly coincide for large W_{Si}.

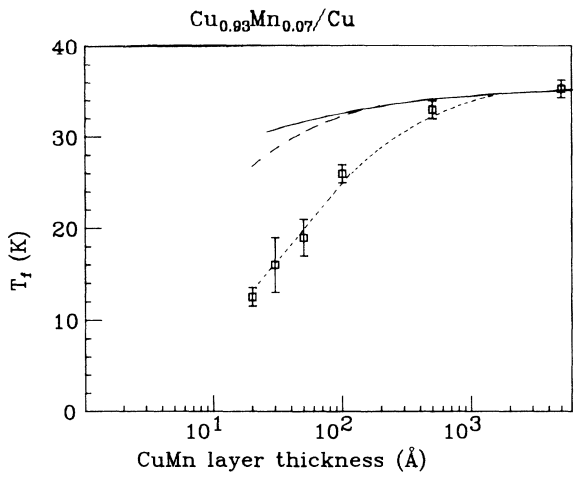

FIG. 18. T_f vs $W_{\text{Cu-Mn}}$ for the $Cu_{0.93}Mn_{0.07}$/Cu MS's. The solid curve indicates the predicted reductions in T_f for the quenched-uniform model. The long-dash and short-dash curves indicate, respectively, the predicted reductions in T_f due solely to boundary layer spreading of 5 and 35 Å, respectively.

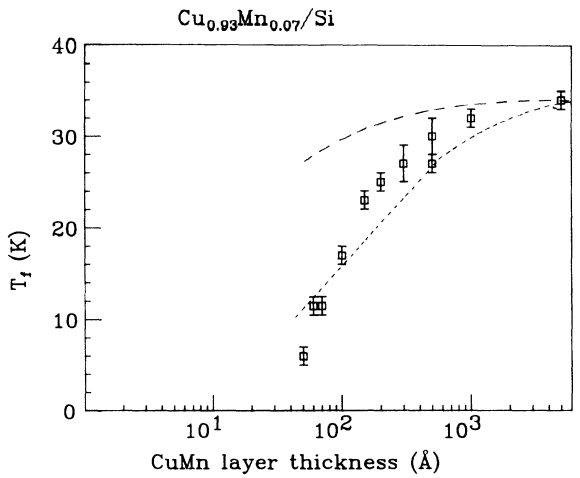

FIG. 19. T_f vs $W_{\text{Cu-Mn}}$ for the $Cu_{0.93}Mn_{0.07}$/Si MS's. The long-dash and short-dash curves indicate, respectively, the predicted reductions in T_f due solely to boundary layer spreading of 10 and 100 Å, respectively.

sition temperature T_f occurs down to $W_{\text{Cu}}=100$ Å; 300 Å of Cu was used to magnetically decouple the SG layers.

Figure 17 shows the variation of T_f with Si thickness W_{Si} for the $Cu_{1-x}Mn_x$/Si MS's. Here T_f remains constant down to 30 Å, below which it begins to shift upward towards the bulk spin-freezing temperature T_f^b for Cu-Mn. In these examples, SAXD measurements showed good layering down to $W_{\text{Si}}=30$ Å, but no layer-

TABLE VII. Collected values of T_f for different values of the Cu-Mn layer width $W_{\text{Cu-Mn}}$ for $Cu_{1-x}Mn_x$/Cu and $Cu_{1-x}Mn_x$/Si MS's with $x=0.04$, 0.07, and 0.14, and for $Cu_{1-x}Mn_x$/Si MS's with $x=0.21$. No samples of $Cu_{1-x}Mn_x$/Cu were made with $x=0.21$. The Cu-Mn layers were magnetically decoupled by 300 Å layers of Cu or 70 Å layers of Si. The listed values of T_f are typically good to ±1 K, but can be as bad as ±5 K for $x=0.21$. Values separated by a slash were taken on two independent samples. Most of the columns contain data from two or more sputtering runs. The column labeled Cu_c represents $Cu_{0.96}Mn_{0.04}$/Cu MS's prepared from a new sputtering target and with the substrates cooled to below room tempeature.

$W_{\text{Cu-Mn}}$ (Å)	T_f (K)							
	4% Mn			7% Mn		14% Mn		21% Mn
	Cu_c	Cu	Si	Cu	Si	Cu	Si	Si
20		6.5		12.5		24		
30		10		16		30.5		
40		11.5			≤2			31/31.5
50	12	12	6.5	19	6	40/40	17	36
60					11.5			40
70	13	14	9.4		11.5	46	28	30
100	16.2	17.4	12	26	17	45	34	41
150			16.5		23			
200		20	18		25	54	50	85
300		20/20	20		27			
400			20.2					105
500	22.8	22/22	21.8	33	27/30	58	53.5	100/98
1 000	22.9		22.4		32			95
5 000	22			35.3	34		59	96/100
10 000						62.5		
Shavings	24	23.2		34		62		100

ing was observed for $W_{Si}=20$ Å; 70 Å of Si was used to magnetically decouple the SG layers.

The χ curves in Fig. 14 show that the SG samples displayed a monotonic downward shift in T_f with decreasing Cu-Mn layer thickness. Figures 18 and 19 show plots of T_f versus $\ln W_{\text{Cu-Mn}}$ for the $Cu_{0.97}Mn_{0.07}$/Cu and $Cu_{0.97}Mn_{0.07}$/Si MS's, respectively. Use of a logarithmic scale for $W_{\text{Cu-Mn}}$ permits display on a single graph of data for $W_{\text{Cu-Mn}}$ ranging from 5000 Å down to 20 Å. Similar graphs for the other $Cu_{1-x}Mn_x$/Cu and $Cu_{1-x}Mn_x$/Si MS's are given elsewhere,[35] and values of T_f for all of the MS's are given in Table VII.

As noted in Sec. II, the bulk values of T_f for target shavings agreed well with the values of T_f for samples with $W_{\text{Cu-Mn}}=5000$ Å; therefore, samples with a thickness of 5000 Å and above are considered to be bulk. Figures 18 and 19 show that deviations from the bulk T_f were observed in both $Cu_{1-x}Mn_x$/Cu and $Cu_{1-x}Mn_x$/Si MS's for $W_{\text{Cu-Mn}}$ as large as 1000 Å.

Over the range of concentrations $x=0.04-0.14$, the microscopic nature of the Cu-Mn SG changes considerably; statistically, the average total number of impurities in the nearest-neighbor (NN) and next-nearest-neighbor (NNN) sites to a selected impurity increases by 350%. These increases in NN and NNN cause the bulk transition temperature T_f to increase by about 250%. The increase in the NNN could also increase the amount of short-range ferromagnetic ordering. Given these changes, it is interesting to examine whether scaling behavior is present in our samples—that is, whether we find a single "universal" curve when values of T_f for a given Mn concentration x are normalized to the bulk value T_f^b for that same x. Figures 20 and 21 show that, to within experimental uncertainty, we find single, but separate, curves for the two different interlayer materials.

In Figs. 20 and 21 we appear to have $T_f \to 0$ K at $W_{\text{Cu-Mn}} \approx 35$ Å and ≈ 10 Å in the $Cu_{1-x}Mn_x$/Si and

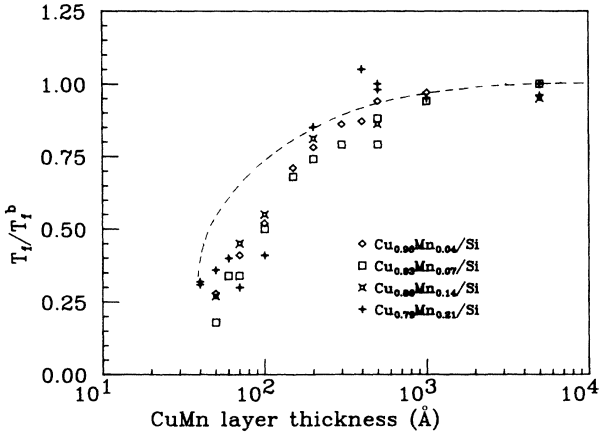

FIG. 20. T_f/T_f^b vs $W_{\text{Cu-Mn}}$ for all of the $Cu_{1-x}Mn_x$/Si MS's. The dashed curve indicates the effective T_f values obtained if the measured values are corrected for an assumed boundary spreading of 10 Å as described in the text.

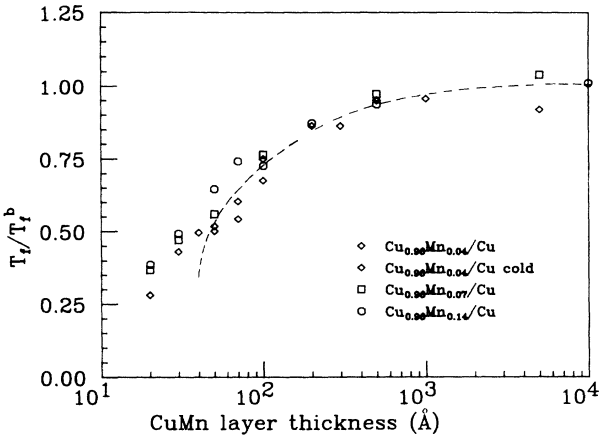

FIG. 21. T_f/T_f^b vs $W_{\text{Cu-Mn}}$ for all of the $Cu_{1-x}Mn_x$/Cu MS's. The dashed curve is the same as in Fig. 20.

$Cu_{1-x}Mn_x$/Cu MS's, respectively. If the data are replotted with the abscissa linear in $W_{\text{Cu-Mn}}$, we still find that $T_f \to 0$ K for $W_{\text{Cu-Mn}} > 0$ Å for the $Cu_{1-x}Mn_x$/Si MS's, but we shall see in Sec. IV D that the data for the $Cu_{1-x}Mn_x$/Cu MS's are perfectly compatible with $T_f \to 0$ K at $W_{\text{Cu-Mn}} \to 0$ Å; in this latter case, the plot in Fig. 21 versus $\ln W_{\text{Cu-Mn}}$ is simply visually misleading.

B. Boundary effects

1. *Decrease in average impurity interaction*

From the fact that the T_f^b for $Cu_{1-x}Mn_x$ increases rapidly with increasing x, it follows that impurity-impurity interactions must play a fundamental role in determining the value of T_f. We have used the uniform-quenched model for an undamped RKKY interaction described in Sec. III B to estimate how large a reduction in T_f occurs simply because, as a Cu-Mn layer becomes thinner, the impurities near the layer surface—which have fewer impurity near neighbors—become a larger fraction of the total number of impurities in the sample. Typical calculated results are shown as the solid curve in Fig. 18. We see that the boundary effect produces much less reduction in T_f than we observe.

2. *Spreading of Mn into the interlayer*

A potentially more important issue is that of spreading of Mn into the Si or Cu interlayers during sputtering, since such spreading reduces the Mn concentration in the Cu-Mn, and thus the expected T_f even if there are no "finite-size effects." We estimate the importance of such effects using Eq. (11) in Sec. III A. The long-dashed curves in Figs. 18 and 19 correspond, respectively, to our best estimates of 5 Å Cu-Mn spreading (total boundary layer width of 10 Å) in the $Cu_{1-x}Mn_x$/Cu MS's, and 10 Å spreading (boundary layer width of 20 Å) in the $Cu_{1-x}Mn_x$/Si MS's. These curves produce, respectively, only about $\frac{1}{3}$ and $\frac{1}{4}$ of the observed decreases in T_f. To

produce the complete decreases requires Cu-Mn spreading of 35 Å in the $Cu_{1-x}Mn_x$/Cu MS's and 100 Å in the $Cu_{1-x}Mn_x$/Si MS's, as indicated by the short-dashed curves in Figs. 18 and 19.

3. *Mixing of Si into Cu-Mn, silicide formation, and correction for Cu_{1-x} Mn_x/Si layer spreading*

The unusually large increases in resistivity of the $Cu_{1-x}Mn_x$/Si MS's as the Cu-Mn layers are made thinner shown in Fig. 6, and the apparently nearly random values of the magnitudes of the susceptibility peaks for these same MS's,[35] both seem to indicate that Si diffusion into the Cu-Mn along grain boundaries and silicide formation are affecting the $Cu_{1-x}Mn_x$/Si MS data. Both phenomena should tend to reduce T_f for a given $W_{\text{Cu-Mn}}$. In the absence of knowledge of the details of either phenomenon, we first ask whether the differences between the $Cu_{1-x}Mn_x$/Si data and the $Cu_{1-x}Mn_x$/Cu data can be explained solely by an additional ≈ 10 Å boundary spreading in the $Cu_{1-x}Mn_x$/Si MS's. The identical dashed curves in Figs. 20 and 21 indicate the "effective T_f" values obtained when the measured values of T_f for the $Cu_{1-x}Mn_x$/Si MS's are *increased* by amounts equivalent to the *decreases* in T_f represented by the long-dashed curve in Fig. 19. Down to $W_{\text{Cu-Mn}} \approx 50$ Å, the dashed curve in Fig. 21 lies close enough to the $Cu_{1-x}Mn_x$/Cu MS data to approximately account for the differences in T_f between the $Cu_{1-x}Mn_x$/Cu and $Cu_{1-x}Mn_x$/Si MS's. However, when extrapolated to still thinner values of $W_{\text{Cu-Mn}}$, the curve falls below the $Cu_{1-x}Mn_x$/Cu data. We attribute this discrepancy at small values of $W_{\text{Cu-Mn}}$ to effects of Si diffusion into the Cu-Mn along grain boundaries, perhaps combined with silicide formation.

C. Finite-size scaling in the $Cu_{1-x}Mn_x$/Cu MS

We have shown elsewhere[7,35] that Eq. (13) can fit the experimental data for either $Cu_{1-x}Mn_x$/Cu or $Cu_{1-x}Mn_x$/Si MS's over the entire range of sample thicknesses studied. For the $Cu_{1-x}Mn_x$/Cu MS's the fit extrapolates to $T_f = 0$ K at a finite-layer width of $W_{\text{Cu-Mn}} \approx 10$ A; for the $Cu_{1-x}Mn_x$/Si MS's, the extrapolation is to $T_f = 0$ K for $W_{\text{Cu-Mn}} \approx 35$ A. Since Eq. (13) is expected to be valid only for T_f near T_f^b, it is not at all obvious why these good fits occur. The significance of the resulting values of $W_{\text{Cu-Mn}}$ for which $T_f = 0$ K is also not clear; in the context of the discussion to follow, we take the value of $W_{\text{Cu-Mn}} \approx 10$ A as an upper bound on the actual Cu-Mn layer width at which $T_f = 0$ K. In the remainder of this paper, we limit our analysis to the expected ranges of validity of given models.

For the reasons discussed in the preceding section, we conclude that the $Cu_{1-x}Mn_x$/Cu MS's more closely approximate the ideal layered SG system than the $Cu_{1-x}Mn_x$/Si MS's. We, therefore, limit further comparisons with theoretical models to the $Cu_{1-x}Mn_x$/Cu MS's. For simplicity, and given the uncertainties in both the data and our knowledge of the width of the Mn penetration into the Cu interlayers, we analyze the "raw" data of Fig. 21, without corrections for the possible perturbing effects just considered in Sec. IV B.

Finite-size scaling arises from the static properties of the system and should be observable only in the asymptotic limit as L approaches the bulk value. The data for Cu interlayers shown in Fig. 21 can be divided into two regimes at $W_{\text{Cu-Mn}} \approx 200$ Å. If we replot these data on a log-log scale as shown in Fig. 22, then when we apply finite-size scaling as embodied in Eq. (13) to the "thick" (i.e., $W_{\text{Cu-Mn}} > 200$ Å) regime for all concentrations of Mn, we obtain the dashed curve of Fig. 22 which yields $\nu = 1.1 \pm 0.3$. If we define the experimental correlation length ξ as the sample width at which size effects become evident, we find from Fig. 22 that $\xi \approx 1000$ Å. These values of ν and ξ agree well with values $\nu = 1.3 \pm 0.2$ and $\xi \approx 2000$ Å obtained by Levy and Ogielski[9] from their nonlinear susceptibility measurements on AgMn.

We note that the uncertainties in the data of Fig. 22 are too large to permit us to isolate the logarithmic correction to finite-size scaling predicted for our thick samples by Fisher and Huse.

Finite-size-scaling analysis predicts rounding of divergent behavior due to restriction of the correlation length in the direction of the reduced dimension. As shown in Fig. 15, we see no obvious evidence of increased rounding in the widths of the normalized dc χ with decreasing $W_{\text{Cu-Mn}}$. This lack of noticeable rounding in the susceptibility is a little disconcerting, since the exponent which determines rounding behavior, Θ, is postulated[1] to be equal to the shift exponent λ, and we have been able to apply our scaling analysis to T_f over a large variation in $W_{\text{Cu-Mn}}$. Two possible explanations for this discrepancy are the following. The samples may be sufficiently strained so that the cusp is already broadened beyond the

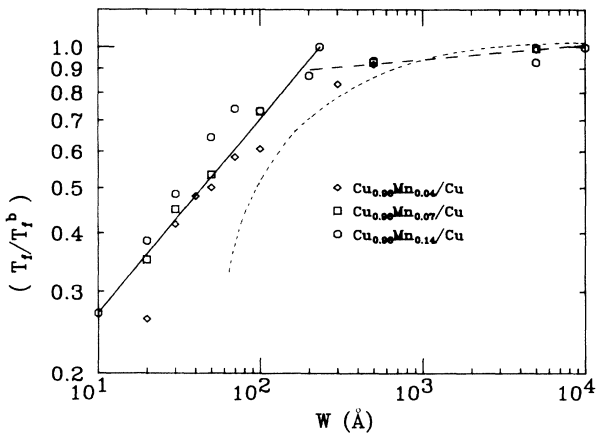

FIG. 22. $\text{Log}(T_f/T_f^b)$ vs $\text{Log}W_{\text{Cu-Mn}}$ for all of the $Cu_{1-x}Mn_x$/Cu MS's studied. The solid line is a fit of the data for $W_{\text{Cu-Mn}} < 200$ Å to Eq. (24). The dashed curve is a fit of the data for $W_{\text{Cu-Mn}} > 200$ Å to Eq. (13). The dotted line indicates the average behavior of the $Cu_{1-x}Mn_x$/Si MS's.

intrinsic effects predicted by finite-size scaling. The linear susceptibility in the spin glass is not divergent, so that the rounding predicted by finite-size scaling may not be observable even in unstrained samples.

D. Fisher-Huse droplet excitation analysis for thin Cu-Mn layers

As the Cu-Mn layer thickness $W_{\text{Cu-Mn}}$ approaches zero, Fisher and Huse[2] predict that far below T_f^b the ratio T_f/T_f^b is given by Eq. (23). If we assume that our measuring time t_m is a constant, then we can rewrite Eq. (23) in the form

$$\ln(T_f/T_f^b)=K\ln W\ , \tag{24}$$

where $K=(\psi_3+\nu_2\theta_3)/1+\nu_2\psi_2)$. Figure 22 shows that our data for all Mn concentrations are compatible with Eq. (24) yielding $K=0.5\pm0.1$. The exponent is a combination of several factors for which we do not have accurate predictions from either simulations or analytical theory, and thus we can make no more detailed comparison with the Fisher-Huse theory.

E. Finite-correlation-length SDW model

In Sec. III we noted that Werner *et al.*[37] have argued that single-crystal Cu-Mn is not a traditional SG, but rather a finite-correlation-length SDW system with a correlation length of about 40 Å. If we assume that this picture applies to our polycrystalline samples with crystallite sizes within an order of magnitude of this correlation length, and that 40 Å is the only correlation length in the system, then we would not expect any significant decrease in T_f until $W_{\text{Cu-Mn}}\approx 40$ Å. In disagreement with this prediction, we find that T_f has already begun to decrease by $W_{\text{Cu-Mn}}\approx 1000$ Å.

For very thin samples, the detailed behavior of T_f is likely to depend upon the orientation of the SDW's. Assuming that these lie along fixed crystallographic directions, some SDW's will have substantial components perpendicular to the layers. We might expect these SDW's to be completely disrupted when the sample thickness becomes smaller than about 40 Å, leading to dramatic effects on T_f. Indeed, in our $Cu_{1-x}Mn_x$/Si MS's, T_f goes to zero at about 35 Å. Thus if these were the only data we had, it would be tempting to relate this thickness to a possible SDW correlation length. However, we do not see similar behavior in our $Cu_{1-x}Mn_x$/Cu MS's, and the possibility of boundary spreading and interdiffusion of Si and Cu provides a plausible explanation for the different behaviors of our $Cu_{1-x}Mn_x$/Si and $Cu_{1-x}Mn_x$/Cu MS's. We thus conclude that our data do not provide direct supporting evidence for the presence of finite-correlation-length SDW's in Cu-Mn.

F. Dynamics of $Cu_{1-x}Mn_x$/Cu MS's

We noted in the Introduction that the T_f in bulk SG's depends weakly on the measuring time t_m. A convenient parameter for describing this variation is the dimensionless quantity

$$k=-(t_m/T_f)(dT_f/dt_m)\ .$$

In bulk $Cu_{1-x}Mn_x$, k is independent of x in our range of concentrations.[41] Thus simple spreading of the Cu-Mn layers in our SG MS's should leave k independent of $W_{\text{Cu-Mn}}$.

For $Cu_{1-x}Mn_x$ well above d_l, k should be small, since decreasing t_m should cause T_f to move only slowly away from its "true" value of $T_f(\infty)$ (e.g., T_f independent of t_m implies $k=0$). In agreement with this expectation, we and our collaborators in the group of Lundgren *et al.* in Uppsala recently found[42] $k\approx 0.005$ for 10 000 A thick films of $Cu_{1-x}Mn_x$ and $t_m\approx 10$ sec. This value of k is compatible with those obtained by others on bulk Cu-Mn.[41]

For $Cu_{1-x}Mn_x$ below its d_l, in contrast, there is no phase transition at $t_m=\infty$, which means that $T_f(\infty)=0$. Since values of T_f measured at finite t_m must then extrapolate to $T=0$ K as $t_m\to\infty$, we would expect k to increase substantially over the value that it has well above d_l. Indeed, we found[42] that k increased by a factor of 5, to a value of ≈ 0.025 for $W_{\text{Cu-Mn}}=20$ A. This behavior is compatible with the finite-size effects inferred in the current paper, but incompatible with simple boundary layer spreading of the Cu-Mn.

V. CONCLUSIONS

We have fabricated and characterized multiplayer samples of the SG $Cu_{1-x}Mn_x$, using interlayers of Si and Cu that were made wide enough to magnetically decouple the SG layers. The sample may thus be considered as a stack of isolated SG layers. SQUID susceptometer measurements of the "dc" susceptibility show that the quasistatic freezing temperature T_f, defined as the temperature of the peak in the susceptibility, shifts rapidly downward with decreasing SG layer thickness, approaching $T=0$ K for very thin samples. The observed shifts are much too large to be explained by a reduction in the average number of magnetic neighbors of magnetic atoms due the finite widths of the SG layers. The shifts can be approximately reproduced by assuming layer spreadings of the Cu-Mn by ≈ 35 Å (corresponding to a total boundary layer width of 70 Å) in the $Cu_{1-x}Mn_x$/Cu MS's or by ≈ 100 Å (200 Å total layer width) in the $Cu_{1-x}Mn_x$/Si MS's; however, sample characterization studies indicate that such large spreadings are unlikely.

Both the characterization and magnetic measurements on MS's with Si interlayers indicate that there is intermixing of the Si and the Cu-Mn, leading to a Cu-Mn boundary spreading of ≈ 10–15 Å. Correcting for a 10 Å spreading brings the $Cu_{1-x}Mn_x$/Si data close to the $Cu_{1-x}Mn_x$/Cu data, at least down to a SG layer thickness of 50 Å. The apparent differences between the $Cu_{1-x}Mn_x$/Cu data and the corrected $Cu_{1-x}Mn_x$/Si data below 50 Å are tentatively attributed to diffusion of the Si into the Cu-Mn along grain boundaries, perhaps coupled with silicide formation.

Samples with Cu interlayers seem to have less Cu-Mn boundary spreading (≤ 5 A) than those with Si interlayers. Their values of T_f should thus be more appropri-

ate for comparison with theoretical models. When the values of T_f for a given $Cu_{1-x}Mn_x$/Cu MS are normalized to the T_f^b for the same x, the data for all x fall on a universal curve. We have shown elsewhere[7,35] that this curve is compatible with the finite-size-scaling model of Eq. (13) for all values of $W_{Cu\text{-}Mn}$, and that the fit to Eq. (13) yields $T_f=0$ K at $W_{Cu\text{-}Mn}\approx 10$ A. This fit is surprising, since finite-size scaling should apply only for T_f near T_f^b. In the present paper we fit the curve in two separate regimes. For $W_{Cu\text{-}Mn}>200$ Å, finite-size scaling yields an exponent that is consistent with independent observations by Levy and Ogielski on nonlinear susceptibility of bulk AgMn. For $W_{Cu\text{-}Mn}<200$ Å, the form of the data is compatible with the predictions of the phenomenological droplet model of Fisher and Huse for a 3D to 2D crossover in Cu-Mn. In this model, $T_f=0$ K only when $W_{Cu\text{-}Mn}=0$ A.

We believe that these results represent the first experimental evidence of crossover from 3D to 2D behavior in a long-range SG.

ACKNOWLEDGMENTS

We would like to thank H. Bouchiat and P. Monod for suggesting the model of Mn spreading discussed in Sec. III A. We would like to acknowledge the assistance of V. Shull, W. Abdul-Razzaq, J. Heckmann, C. Bruch, and D. Gregory in the fabrication and characterization of the samples. The work was supported in part by National Science Foundation Grant Nos. DMR 8303206 and DMR 8819429 and by the MSU Center for Fundamental Materials Research.

*Present address: Physics Department, UCLA, Los Angeles, CA 90024.

†Present address: Institut de Physics Experimental, Universite de Lausanne, CH-1015 Lausanne, Switzerland.

[1]M. N. Barber, in *Phase Transitions and Critical Phenomena,* edited by C. Domb and J. L. Lebowitz (Academic, New York, 1983), Vol. 8.

[2]D. S. Fisher and D. A. Huse, Phys. Rev. B **36**, 8937 (1987).

[3]K. Binder and A. P. Young, Rev. Mod. Phys. **58**, 801 (1986).

[4]H. Lutz, J. D. Gunton, H. K. Schurmann, J. E. Crow, and T. Mihalisin, Solid State Commun. **14**, 1075 (1974).

[5]M. Farle and K. Baberschke, Phys. Rev. Lett. **58**, 511 (1987).

[6]K. Binder, in *Phase Transitions and Critical Phenomena,* Ref. 1.

[7]J. A. Cowen, G. G. Kenning, and J. M. Slaughter, J. Appl. Phys. **61**, 4080 (1987); G. G. Kenning, J. M. Slaughter, and J. A. Cowen, Phys. Rev. Lett. **59**, 2596 (1987); J. A. Cowen, G. G. Kenning, and J. Bass, J. Appl. Phys. **64**, 5781 (1988).

[8]K. H. Fischer, in *Metals, Electronic Transport Phenomena,* Vol. 15a of *Landolt-Börnstein Tables,* New Series Group III, edited by K. H. Hellwege (Springer-Verlag, Berlin, 1982), p. 289.

[9]L. P. Levy and A. T. Ogielski, Phys. Rev. Lett. **57**, 3288 (1986).

[10]A. Fert and P. M. Levy, Phys. Rev. Lett. **44**, 1538 (1980).

[11]N. de Courtenay, H. Bouchiat, H. Hurdequint, and A. Fert, J. Phys. (Paris) **47**, 1507 (1986).

[12]C. Dekker, A. F. M. Arts, and H. W. de Wijn, Phys. Rev. Lett. **61**, 1780 (1988).

[13]D. D. Awschalom, J. M. Hong, L. L. Chang, and G. Grinstein, Phys. Rev. Lett. **59**, 1733 (1987).

[14]J. D. Reger and A. P. Young, Phys. Rev. B **37**, 5493 (1988).

[15]A. Fert, N. de Courtenay, and H. Bouchiat, J. Phys. (Paris) **49**, 1173 (1988).

[16]J. Vranken, C. Van Haesendonck, H. Vloeberghs, and Y. Brunseraede, Phys. Scr. **T25**, 348 (1989).

[17]R. Stubi, J. A. Cowen, and J. Bass (unpublished).

[18]S. M. Durbin, J. E. Cunningham, and C. P. Flynn *et al.,* J. Phys. F **17**, L59 (1987); J. L. Makous, C. M. Falco, R. Vaglio, and A. Cucolo, Jpn. J. Appl. Phys. **26**, Suppl. 26-3, 1467 (1987).

[19]M. B. Stearns, C. H. Lee, and T. L. Groy, Phys. Rev. B **40**, 8256 (1989).

[20]A. Guinier, *X-ray Diffraction* (Freeman, San Francisco, 1963).

[21]B. D. Cullity, *Elements of X-ray Diffraction* (Addison-Wesley, Reading, MA, 1956).

[22]I. K. Schuller, Phys. Rev. Lett. **44**, 1597 (1980).

[23]A. Segmuller and A. E. Blakeslee, J. Appl. Cryst. **6**, 19 (1973).

[24]D. B. McWhan, in *Synthetic Modulated Structures,* edited by L. L. Chang and B. C. Giessen (Academic, New York, 1982), p. 43, and references therein.

[25]W. Sevenhans, M. Gijs, Y. Bruynseraede, H. Homma, and I. K. Schuller, Phys. Rev. B **34**, 5955 (1986).

[26]J. M. Slaughter, Ph.D. thesis, Michigan State University, 1987.

[27]W. B. Pearson, *Handbook of Lattice Spacings and Structures of Metals* (Pergamon, New York, 1958).

[28]J. M. Slaughter, W. P. Pratt, Jr., and P. A. Schroeder, Rev. Sci. Instrum. **60**, 127 (1989).

[29]G. Betz and G. K. Wehner, Top. Appl. Phys. **52**, 11 (1981).

[30]W. D. Westwood, Mater. Res. Bull. **13**, 46 (1988).

[31]M. Hansen, *Constitution of Binary Alloys,* 2nd ed. (McGraw-Hill, New York, 1958).

[32]D. Lazarus, in *Solid State Physics,* edited by F. Seitz and D. Turnbull (Academic, New York, 1960), Vol. 10, p. 71; Diffusion and Defect Data **44-45**, 145 (1986).

[33]C. Fierz, R. Stubi, and W. P. Pratt (unpublished).

[34]L. J. van de Pauw, Philips Res. Rep. **13**, 1 (1958).

[35]G. G. Kenning, Ph.D. thesis, Michigan State University, 1988.

[36]J. Bass, in *Metals, Electronic Transport Phenomena,* Vol. 15a of *Landolt-Börnstein Tables,* New Series Group III, Ref. 8, p. 139.

[37]S. A. Werner, J. J. Rhyne, and J. A. Gotaas, Solid State Commun. **56**, 457 (1985).

[38]U. Larsen, Phys. Rev. B **33**, 4803 (1986).

[39]D. C. Vier and S. Schultz, Phys. Rev. Lett. **54**, 150 (1985).

[40]S. Nagata, P. H. Keesom, and H. R. Harrison, Phys. Rev. B **19**, 1633 (1979).

[41]J. L. Tholence, Physica **B126**, 157 (1984).

[42]L. Sandlund, P. Granberg, L. Lundgren, P. Norblad, P. Svedlindh, J. A. Cowen, and G. G. Kenning, Phys. Rev. B **40**, 869 (1989); P. Granberg, P. Nordblad, P. Svedlindh, L. Lundgren, R. Stubi, G. G. Kenning, D. L. Leslie-Pelecky, J. Bass, and J. Cowen, J. Appl. Phys. **67**, 525 (1990).

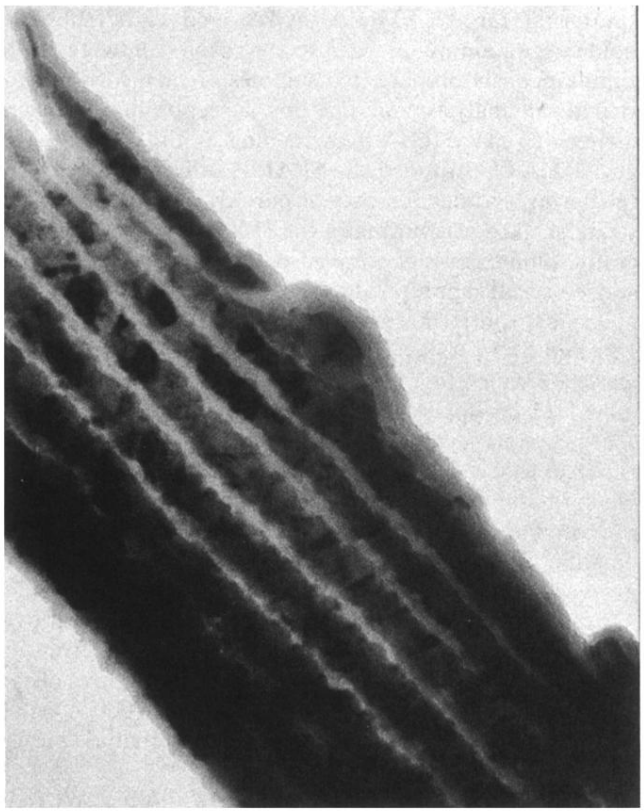

FIG. 3. Bright-field image of a $Cu_{0.93}Mn_{0.07}$/Si (200 Å/70 Å) MS taken on the TEM. Magnification = 190 K.

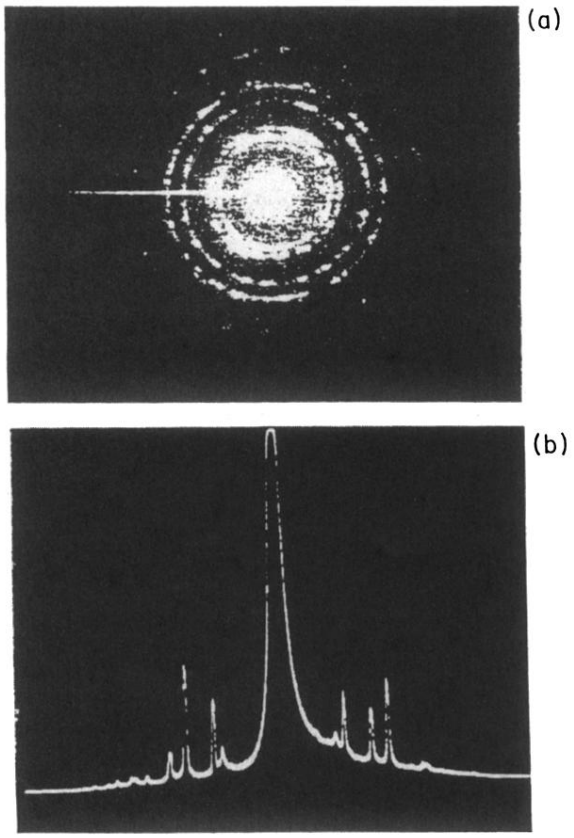

FIG. 8. (a) SAD pattern of a $Cu_{0.86}Mn_{0.14}$/Cu (200 Å/300 Å) MS taken on the FE-STEM. (b) Line scan of the SAD pattern of (a).